Nano Research 2016, 9(12): 3559–3597
DOI 10.1007/s12274-016-1224-5
Review Article
ISSN 1998-0124
CN 11-5974/O4

Lattice vibrations and Raman scattering in two-dimensional layered materials beyond graphene

Xin Lu[1,§], Xin Luo[2,3,§], Jun Zhang[4], Su Ying Quek[2,3] (✉), and Qihua Xiong[1,5] (✉)

[1] *Division of Physics and Applied Physics, School of Physical and Mathematical Sciences, Nanyang Technological University, Singapore 637371, Singapore*
[2] *Department of Physics, National University of Singapore, 2 Science Drive 3, Singapore 117551, Singapore*
[3] *Centre for Advanced 2D Materials, National University of Singapore, 6 Science Drive 2, Singapore 117546, Singapore*
[4] *State Key Laboratory of Superlattices and Microstructures, Institute of Semiconductors, Chinese Academy of Sciences, Beijing 100083, China*
[5] *NOVITAS, Nanoelectronics Centre of Excellence, School of Electrical and Electronic Engineering, Nanyang Technological University, Singapore 639798, Singapore*
[§] *These authors contributed equally to this work.*

Received: 16 May 2016
Revised: 10 July 2016
Accepted: 18 July 2016

KEYWORDS

phonon,
lattice vibration,
Raman spectroscopy,
two-dimensional,
transition metal dichalcogenide,
black phosphorus

ABSTRACT

We review lattice vibrational modes in atomically thin two-dimensional (2D) layered materials, focusing on 2D materials beyond graphene, such as group VI transition metal dichalcogenides, topological insulator bismuth chalcogenides, and black phosphorus. Although the composition and structure of those materials are remarkably different, they share a common and important feature, i.e., their bulk crystals are stacked via van der Waals interactions between "layers", while each layer is comprised of one or more atomic planes. First, we review the background of some 2D materials (MX_2, M = Mo, W; X = S, Se, Te. Bi_2X_3, X = Se, Te. Black phosphorus), including crystalline structures and stacking order. We then review the studies on vibrational modes of layered materials and nanostructures probed by the powerful yet nondestructive Raman spectroscopy technique. Based on studies conducted before 2010, recent investigations using more advanced techniques have pushed the studies of phonon modes in 2D layered materials to the atomically thin regime, down to monolayers. We will classify the recently reported general features into the following categories: phonon confinement effects and electron–phonon coupling, anomalous shifts in high-frequency intralayer vibrational modes and surface effects, reduced dimensionality and lower symmetry, the linear chain model and the substrate effect, stacking orders and interlayer shear modes, polarization dependence, and the resonance effect. Within the seven categories, both intralayer and interlayer vibrational modes will be discussed. The comparison between different materials will be provided as well.

Address correspondence to Su Ying Quek, phyqsy@nus.edu.sg; Qihua Xiong, qihua@ntu.edu.sg

1 Introduction

Recent interest in layered materials is mostly driven by the desire to understand the properties of atomically thin forms, because ultra-thin flakes can sometimes achieve what bulk crystals cannot accomplish, such as unique properties and better performance. Experimental and theoretical studies on ultra-thin two-dimensional (2D) layered materials, including graphene, topological insulators, transition metal dichalcogenides (TMDs), and black phosphorus, are motivated by the discovery of fascinating properties and novel phenomena in mono- and few-layer systems, as well as 2D-based heterostructures [1–9]. For instance, the quantum Hall effect has been observed in graphene at room temperature [10]. A 2D topological insulator is also known as a quantum spin Hall insulator [11, 12]. In monolayer MoS_2 and WS_2 (typical group VI TMDs), strong photoluminescence (PL) in the visible range has been reported [13–15]. Compared with TMDs, the high carrier mobility of black phosphorus has made it a popular material in the recent development of 2D field effect transistors (FETs) [16, 17]. Besides, the anisotropic behavior resulting from the crystal structure has made black phosphorus very attractive for applications in optoelectronics [18, 19].

Lattice vibrations, whose quanta are phonons, play an important role in the intriguing properties and observed phenomena in 2D materials, particularly their thermal conductivity and electrical conductivity. A well-known example is the FET mobility of 2D materials, which is affected by the acoustic, optical, and surface/interface phonon scattering [20, 21]. Meanwhile, the optical observation of valley polarization in TMDs is usually conducted at low temperature to weaken the inter-valley phonon scattering [22–24]. Thus, it is important to investigate and understand the properties of phonons.

Very recently, several review papers have been published, discussing the phonon characteristics of 2D materials beyond graphene [25–28]. Each of these reviews has provided a different point of view on this important topic. For example, Ji et al. focused on the interlayer vibrational modes [27], while Zhang et al. provided a detailed overview of Raman spectra for a variety of layered materials [28]. Here, we review studies on lattice vibrational modes in 2D layered materials beyond graphene, encompassing theoretical calculations and experimental investigations based on Raman spectroscopy. After introducing the structure and stacking, we first review previous studies of Raman scattering for a variety of layered materials and nanostructures. Thereafter, we discuss the general features of lattice vibrations in atomically thin 2D layered materials, in the following order: (1) phonon confinement effects and electron–phonon coupling; (2) anomalous shifts and surface effects; (3) reduced dimensionality and lower symmetry; (4) the linear chain model and the substrate effect; (5) stacking orders and interlayer shear modes; (6) polarization dependence; (7) the resonance effect. We will be focusing on group VI TMDs (MX_2, M = Mo, W; X = S, Se, Te), while Bi_2X_3 (X = Se or Te) and black phosphorus will be discussed as well.

2 Background on Raman spectroscopy and 2D materials beyond graphene

2.1 Structure and stacking order in group VI TMDs, Bi_2X_3 (X = Se or Te), and black phosphorus

Each layer of group VI TMDs MX_2 (M = Mo, W; X = S, Se, Te) consists of X–M–X tri-atomic planes, such that a monolayer can also be called a "tri-layer" (1 TL) [3]. In monolayer black phosphorus (i.e., phosphorene), we can consider the atoms to be in one puckered atomic layer [29]. Compared with TMDs and phosphorene, which are relatively simple in terms of their crystal structure, the stable rhombohedral Bi_2X_3 (X = Se or Te) has five atomic planes in a single layer [30, 31]. Thus, a monolayer Bi_2X_3 can also be called a quintuple layer (1 QL).

There is a structural polytypism among group VI TMDs MX_2 (M = Mo, W; X = S, Se, Te). For S- and Se-based MX_2 (M = Mo, W; X = S, Se), the most common and stable phase is 2H, with H referring to the hexagonal structure and "2" to the number of layers per unit cell [2]. For MTe_2 (M = Mo, W), the large size of the telluride atom distorts the structure, stabilizing the 1T′ phase [32, 33]. Other common phases of group VI TMDs include 1T and 3R. While the 1T phase has been reported to be metastable in

MoS_2 [34] and $MoSe_2$ [35], detailed dynamical studies show that a perfect 1T TMD monolayer has imaginary modes, and a distorted phase (d1T or 1T′ or ZT) is more stable [36]. Experimentally, dynamic rearrangements of W atoms in the ZT phase WS_2 have been observed using transmission electron microscopy, with the reorientation of zigzag chains and the formation of tetramer clusters. Calculations show that the energy barrier for reorienting the zigzag chains is very low, while negative charge is required to stabilize the tetramer phase. The negative charge weakens the W–S bonds, while the formation of tetramers strengthens the W–W bonds [37].

It is instructive to compare the above descriptions of TMD structural polytypes with the crystal structure of graphene. Graphene has a simple crystal structure: Its monolayer form has only one atomic layer and the carbon atoms are hexagonally arranged within the same plane as well. In a few-layer graphene, there are two types of stacking orders, the Bernal (AB) stacked and the rhombohedral (ABC) stacked graphene. By comparison, 2H-MoS_2 and 3R-MoS_2 can be regarded as AB-stacked and ABC-stacked, respectively. The former has two layers per unit cell, and the latter has three [38]. In order to minimize the amount of information needed for the complete description of a unit cell, the space group is introduced. Materials with the same space group share the same Raman tensors. Space groups and stacking orders of common 2D layered materials are summarized in Table 1.

We consider MX_2 (M = Mo, W; X = S, Se) as examples for further illustrating the space group and stacking orders. Schematics in Fig. 1(a) show the corresponding crystal structures of 1T-, 2H-, and 3R-stacked tri-layers, belonging to the space groups D_{3d}^3, D_{3h}^1, and D_{3v}^1, respectively. It is worth noting that the monolayer counterparts of 2H and 3R are the same, also referred to as 1H. In contrast, the spatial inversion symmetry is preserved in the 1T stacking, but it is broken in the 1H structure. The difference between 2H and 3R starts from the bilayer. Besides the layer shift, which also occurs in the 3R phase, the N^{th} layer of the 2H stacking is rotated with respect to the $(N-1)^{\text{th}}$ layer, as shown in Fig. 1(a). The 3R stacking is noncentrosymmetric from monolayer (1 L) to the bulk, giving rise to the valley polarization regardless of the thickness [39]. In contrast, the 2H stacking with an even number of layers possesses an inversion symmetry point, while that with an odd number of layers is noncentrosymmetric.

During the past year, interest has been growing in $MoTe_2$ and WTe_2, especially in the non-2H phases. For example, MTe_2 (M = Mo, W) with 1T′ stacking has been demonstrated to be important in the quantum spin Hall effect [33]. Comparison between 1T and 1T′ phases, in both the side and top views, is shown in Fig. 1(b), with 2H shown as a reference. The major difference is that M atoms (M = Mo, W) in the 1T′ stacking are distorted, which allows the formation of one-dimensional zigzag chains (along the blue dashed line in Fig. 1(b)).

Table 1 Space group of graphene, black phosphorus, MX_2 (M = Mo, W; X = S, Se), and Bi_2X_3 (X = Se, Te) under AB and ABC stacking orders. "Odd (even) number of layers" is abbreviated to "odd (even) *N*" in the table

		AB stacking		ABC stacking		AB/ABC [a]
	Single layer	Odd *N* $N = 3, 5, 7\ldots$	Even *N* $N = 2, 4, 6\ldots$	Odd *N* $N = 3, 5, 7\ldots$	Even *N* $N = 2, 4, 6\ldots$	Bulk
Multi-layered graphene	D_{6h}^1	D_{3h}^1	D_{3d}^3	D_{3d}^3	D_{3d}^3	D_{6h}^4 / D_{3d}^5
Black phosphorus [b]	D_{2h}^7	D_{2h}^7	D_{2h}^{11}	—	—	D_{2h}^{18}
MX_2 (M = Mo, W; X = S, Se)	D_{3h}^1	D_{3h}^1	D_{3d}^3	C_{3v}^1	C_{3v}^1	D_{6h}^4 / C_{3v}^5
Bi_2X_3 (X = Se, Te)	D_{3d}^3	—	—	D_{3d}^3	D_{3d}^3	D_{3d}^5

[a] For those having both stacking orders, the corresponding space groups in the bulk are listed in the sequence: AB/ABC. For those only possessing one stable stacking, the space group in the bulk is of the same stacking as that in a few-layer system. For example, black phosphorus in the bulk is AB-stacked, while Bi_2X_3 (X = Se, Te) in the bulk is ABC-stacked.

[b] The AB stacking in black phosphorus is different from the definition of AB stacking in Ref. [38], which is consistent with the other AB-stacked materials listed here.

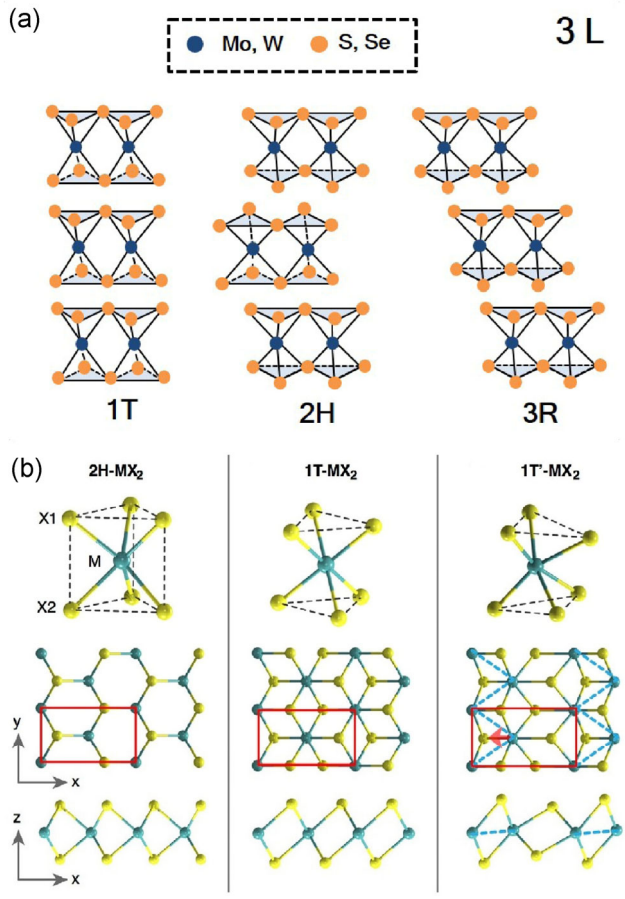

Figure 1 Structural polytypism in MX_2 (M = Mo, W; X = S, Se, Te). (a) Tri-layer MX_2 (M = Mo, W; X = S, Se) with 1T, 2H, and 3R stacking configurations. (b) Comparison of 2H, 1T, and 1T' structures of monolayer MTe_2 (M = Mo, W). Reproduced with permission from Ref. [33], © American Association for the Advancement of Science 2014.

2.2 Raman spectroscopy as a non-destructive tool for probing nanostructures

Raman spectroscopy is an important, versatile, and non-destructive method to probe the vibrational and electronic properties of solid materials [40–42], either of bulk crystals or of nanostructures. Take carbon as an example. Many Raman spectroscopy studies have been performed on graphite, disordered/amorphous carbon, and diamond-like structures. The frequency, intensity, and width of the Raman peaks from Raman spectra can be analyzed via theory/model and correlated to size, defects, and chemical bonding [43, 44]. In 2D carbon, such as atomically thin graphene, Raman spectroscopy can be much more revealing, and can be used to study edge effects, stacking geometries, electron-phonon coupling, electron/hole doping, and interlayer coupling. The detailed interpretation of these phenomena can be found in Ref. [45–47].

Carbon nanotubes are typical 1D carbon structures. Their *(n, m)* values, diameter, and chirality, which are related to the semiconducting versus metallic behavior, can be investigated using Raman spectroscopy [48–50]. Compared with graphene, one-dimensional (1D) nanostructures have more variables to probe, such as the antenna effect owing to the 1D anisotropy nature [51, 52]. Besides carbon nanotubes, other well-known 1D nanostructures, including nanowires, nanorods, and nanobelts have been widely investigated using Raman spectroscopy. Dependence of electron–phonon coupling and quantum confinement on size and excitation laser's wavelength has been widely studied for 1D nanostructures [53–60]. Other interesting phenomena, such as the laser-induced Fano resonance and surface phonons, have also been reported [61–63].

Raman scattering is a process in which incident light is inelastically scattered by phonons [64, 65]. The sample undergoes a light-induced transition between vibrational states. Raman scattering can be divided into Stokes and anti-Stokes scattering. Stokes scattering occurs when the energy of the final vibrational state is higher than that of the initial state, implying that the scattered photons have lower energy than the incident photons. The energy difference between the incident and scattered photons is usually known as the Raman shift in the Raman spectroscopy literature, and is reported in the units of cm^{-1}. Similarly, anti-Stokes scattering occurs when the scattered photons have higher energy than the incident photons, yielding a negative Raman shift. In general, incident photons excite the system to a virtual state before relaxing into the final state. This is called non-resonant Raman scattering. At times, such as when the excitation laser's energy resonates with an optical transition, the system is excited into a real electronic excited state. In this case, resonant Raman scattering is said to occur [66]. In this review, we focus on non-resonant Raman scattering. Thereafter, all of the Raman processes in the text refer to the non-resonant Raman scattering process, unless specifically stated.

Experimentally, lasers used in Raman spectroscopy usually have the energy in the range of 1–4 eV, with a wave vector on the order of 10^5 cm^{-1} in the sample. Because the energy of the scattered light only slightly differs from that of the incident light, phonons involved in Raman scattering must have wavelengths on the order of 10^5 cm^{-1}, owing to the conservation of energy and momentum. However, the size of a typical Brillouin zone is on the order of 10^8 cm^{-1}. Therefore, in first-order Raman scattering processes, in which only one phonon is involved, Raman scattering can only excite phonons near the Brillouin zone center (the Γ point); these phonons are also known as long-wavelength phonons [66–68].

The experimental observation of a given phonon mode in Raman spectroscopy depends on the symmetry selection rules as well as on the scattering geometry. A given phonon mode can be observed using Raman scattering spectroscopy only when $\left|\boldsymbol{e}_{\mathrm{i}}\cdot\tilde{\boldsymbol{R}}\cdot\boldsymbol{e}_{\mathrm{s}}\right|^2$ has a nonzero value, where $\boldsymbol{e}_{\mathrm{i}}$ is the polarization vector of the incident light, $\boldsymbol{e}_{\mathrm{s}}$ is that of the scattered light, and $\tilde{\boldsymbol{R}}$ is the second-rank polarizability tensor, commonly called the Raman tensor. The quantity $\boldsymbol{e}_{\mathrm{i}}\cdot\tilde{\boldsymbol{R}}\cdot\boldsymbol{e}_{\mathrm{s}}$ is given by [69]

$$\boldsymbol{e}_{\mathrm{i}}\cdot\tilde{\boldsymbol{R}}\cdot\boldsymbol{e}_{\mathrm{s}}=\begin{pmatrix}x & y & z\end{pmatrix}\begin{pmatrix}\alpha_{xx} & \alpha_{xy} & \alpha_{xz}\\ \alpha_{yx} & \alpha_{yy} & \alpha_{yz}\\ \alpha_{zx} & \alpha_{zy} & \alpha_{zz}\end{pmatrix}\begin{pmatrix}x\\ y\\ z\end{pmatrix} \quad (1)$$

The parallel-polarized $\bar{z}(xx)z$ configuration and the cross-polarized $\bar{z}(xy)z$ configuration are two widely used polarization configuration setups for 2D layered nano materials on Raman spectroscopy. In this notation, the z axis corresponds (in many instances) to the out-of-plane direction of the nanosheet samples. The z axis is also parallel to the directions in which the incident and scattered light beams travel. The x and y axes are in the basal plane, and the angle between these axes is 90°. The difference between both configurations is in the polarization vector of the scattered light beam $\boldsymbol{e}_{\mathrm{s}}$: For $\bar{z}(xx)z$, $y = z = 0$, and x is non-zero; For $\bar{z}(xy)z$, the incident light is polarized along the x direction, while the outgoing scattered light beam is polarized along the y direction.

The Raman tensor $\tilde{\boldsymbol{R}}$ is related to the crystal's symmetry, and the Raman-active vibrational modes can be predicted based on the group theory analysis, using the irreducible representation of the zone center phonons, which are derived from knowing the material's space group (Table 1) [66]. The irreducible representations of the zone center phonons for 2H-MX_2 (M = Mo, W; X = S, Se), Bi_2X_3 (X = Se, Te), and black phosphorus are summarized in Table 2. In bulk 2H-MX_2 (M = Mo, W; X = S, Se) crystals, the primitive unit cell consists of 2 layers, i.e., 6 atoms. Thus, there are 18 Brillouin zone center (Γ) phonons (3 * number of atoms), with 3 acoustic phonons and 15 optical phonons. In addition, the E symmetry modes in the bulk 2H-MX_2 have 2-fold degeneracy. Among these modes, only A_{1g}, E_{1g}, and $2E_{2g}$ are Raman-active modes. When the thickness decreases to a few layers or a monolayer, two scenarios should be considered, owing to the different symmetries between films with odd and even number of layers (see Table 1). For example, the Raman-active modes in the bilayer are $3A_{1g}$ and $3E_g$; while those in the monolayer are $E'' + A_1' + 2E'$. Note that the mode at ~408 cm^{-1} is A_1' in monolayer, owing to the change in symmetry, although the corresponding mode in 2 L is still A_{1g}. Similarly, the Raman-active modes in Bi_2X_3 (X = Se, Te) are $2E_g+2A_{1g}$, $5(A_{1g}+E_g)$, and $2(A_{1g}+E_g)$ in the bulk, bilayer, and monolayer, respectively. The interlayer vibrational modes from bulk Bi_2X_3 are excluded in the irreducible representation of the zone center phonons. In the bulk black phosphorus, six of the twelve vibrational modes are Raman-active modes: B_{1g}, B_{2g}, $2A_g$, and $2B_{3g}$. Because samples with odd and even numbers of layer(s) belong to the same space group, the irreducible representation of Raman-active modes at the Γ point is $N(2A_g+2B_{3g}+B_{1g}+B_{2g})$, with N being the number of layers.

2.3 Theoretical prediction of Raman spectra

In the Born–Oppenheimer approximation, nuclei move on the potential energy surface, which is the sum of the electronic energy and the nuclear repulsion energy. Because electronic excitations are negligible at room temperature, the ground state electronic energy determines the potential energy surface and the vibration frequencies of nuclei around their equilibrium positions. Therefore, the frequency of phonons can be calculated within the framework of density functional theory

Table 2 Irreducible representations of the zone center phonons in 2H-MX_2 (M = Mo, W; X = S, Se), Bi_2X_3 (X = Se, Te), and black phosphorus. "Odd (even) number of layers" is abbreviated to "Odd (even) *N*" in the table

Material	Thickness	Irreducible representations
2H-MX_2 (M = Mo, W; X = S, Se)	Bulk	$\Gamma = A_{1g} + 2A_{2u} + B_{1u} + 2B_{2g} + E_{1g} + 2E_{1u} + E_{2u} + 2E_{2g}$
	Odd *N* N = 1, 3, 5…	$\Gamma = \frac{3N-1}{2}(A_1' + E'') + \frac{3N+1}{2}(A_2'' + E')$
	Even *N* N = 2, 4, 6…	$\Gamma = \frac{3N}{2}(A_{1g} + A_{2u} + E_g + E_u)$
Bi_2X_3 (X = Se, Te)	Bulk	$\Gamma = 3E_u + 3A_{2u} + 2E_g + 2A_{1g}$
	Odd *N* N = 1, 3, 5…	$\Gamma = \frac{5N-1}{2}(A_{1g} + E_g) + \frac{5N+1}{2}(A_{2u} + E_u)$
	Even *N* N = 2, 4, 6…	$\Gamma = \frac{5N}{2}\left(A_{1g} + A_{2u} + E_g + E_u\right)$
Black phosphorus	Bulk	$\Gamma = 2A_g + 2B_{3g} + 2B_{1u} + 2B_{2u} + A_u + B_{1g} + B_{2g} + B_{3u}$
	Thin layer N = 1, 2, 3, 4…	$\Gamma = N(2A_g + 2B_{3g} + 2B_{1u} + 2B_{2u} + A_u + B_{1g} + B_{2g} + B_{3u})$

(DFT) near the equilibrium geometry by solving the secular equation [70]

$$\det\left|D_{li,kj}(q)\Big/\sqrt{M_l M_k} - \omega^2(q)\delta_{lk}\delta_{ij}\right| = 0 \tag{2}$$

with the dynamical matrix defined as

$$D_{li,kj}(q) = \sum_{\beta} \underbrace{\partial^2 E/(\partial u_{li}^{\alpha}\partial u_{kj}^{\beta})}_{\Phi_{li,kj}^{\alpha\beta}} \exp[i\boldsymbol{q}(\boldsymbol{R}_{\beta} - \boldsymbol{R}_{\alpha})] \tag{3}$$

where u_{li}^{α} is the *i*-th direction component of the atomic displacement of atom *l* in cell α (which can be set to 0), and u_{kj}^{β} is the *j*-th direction component of the atomic displacement of atom *k* in cell *β*. $\boldsymbol{R}_{\alpha}$ and $\boldsymbol{R}_{\beta}$ are the position vectors of cells *α* and *β*, respectively. $\boldsymbol{q}$ is the wave vector of the phonon and *E* is the ground state electronic energy. M_l and M_k are, respectively, the atomic masses of the atoms *l* and *k*. The force constants $\Phi_{li,kj}^{\alpha\beta}$ in the dynamical matrix can be obtained either in the supercell direct approach using finite difference methods, or from the linear response theory [71, 72].

For most layered materials, the *Γ* point phonon mode can be described classically by the linear chain model, based on Hooke's law, with intralayer and interlayer force constants *k* (which are determined by quantum mechanical effects). The dynamical equation for the normal mode of the *n*-th atom can be simplified as $M_n \frac{\mathrm{d}^2 u_n}{\mathrm{d}t^2} = -\sum_m k_{nm}(u_m - u_n)$. This expression can be further simplified by considering the crystal symmetry and the relations between the eigenvectors for each vibration mode. Analytical formulae relating the frequencies and force constants can thus be derived, and the force constants can be obtained by fitting the results of DFT calculations or experimentally measured Raman frequencies [67, 73].

Within the Placzek approximation (i.e., assuming that the intensity of the light scattered by a system with vibrating nuclei is the same for each nuclear configuration as the intensity of the light scattered by a system with nuclei in the fixed configuration), if the incident frequency of the laser light is smaller than any absorption frequency but much larger than the Raman transition frequency, the intensity of the Stokes Raman peak can be calculated as $I^k = \left|\boldsymbol{e}_{\mathrm{i}} \cdot \tilde{\boldsymbol{R}}^k \cdot \boldsymbol{e}_{\mathrm{s}}\right|^2 \propto \frac{(n_k+1)}{\omega_k}\left|\sum_{\alpha\beta} \boldsymbol{e}_{\mathrm{i}\alpha}\boldsymbol{e}_{\mathrm{s}\beta}P_{\alpha\beta,k}\right|^2$, where $\tilde{\boldsymbol{R}}^k$ is the Raman tensor, $P_{\alpha\beta,k}$ is the derivative of the electronic polarizability tensor with respect to the normal coordinates for mode *k*, and *n* is the Bose–Einstein distribution $n_k = 1/\{\exp(\hbar\omega_k/k_B T) - 1\}$ [71]. For the anti-Stokes process, n_k + 1 is replaced by n_k. The

quantity $P_{\alpha\beta,k}$ can be calculated within the empirical bond polarizability model, which we will discuss in detail later. In first principles calculations, $P_{\alpha\beta,k}$ is obtained using the density functional perturbation theory and using the formula $P_{\alpha\beta,k}=\sum_{l\gamma}\frac{\partial^3 E_{tot}}{\partial\varepsilon_m\partial\varepsilon_n\partial u_{l\gamma}}\chi^k_{l\gamma}$, where ε is the electric field, $\frac{\partial}{\partial u_{l\gamma}}$ refers to the derivative (of the polarizability $\frac{\partial^2 E_{tot}}{\partial\varepsilon_m\partial\varepsilon_n}$) with respect to the γ–th spatial coordinate of the atom l, and $\chi^k_{l\gamma}$ is the displacement of the atom l in the γ direction for the eigenmode k [74]. Note that for resonant Raman scattering, in which the laser excitation wavelength matches one of the optically allowed transitions, the above formula is no longer valid because the electron-phonon coupling can significantly enhance the Raman intensities [75, 76].

First principles DFT calculations of the phonon properties of 2D layered materials revealed that the local density approximation (LDA) exchange correlation functional satisfactorily describes a variety of layered materials [77–80]. Compared with the phonon frequencies calculated using existing van der Waals (vdW) functionals [81, 82], or functionals with dispersion correction (PBE-D2) [83], the LDA-calculated frequencies yield the best correspondence with experiments, even for the ultralow interlayer vibrational frequencies [29, 73, 84], where the vdW functionals may not even yield a smooth trend for the frequencies. These results are surprising to some extent, because the LDA does not take into account the vdW interaction. The good agreement between the experimental and LDA-calculated frequencies shows that the curvature of the potential energy surface close to the equilibrium is satisfactorily described by the LDA, even though this may be fortuitous. These results also show that there is room for further improvement of current vdW functionals, to better describe the curvature of the potential energy surface. The accurate description of the ultralow frequency interlayer modes will be an important benchmark in designing new functionals. Furthermore, as we will discuss in Section 3.4, high-level quantum Monte Carlo calculations also do not seem to perform better than the DFT LDA in predicting the force constants.

It is noted that spin-orbit coupling (SOC) plays an important role in the electronic structure of TMDs and topological insulators such as Bi_2X_3 (X = Te, Se). SOC was found not to affect the structural properties of these materials, but to be important for the phonon frequencies, especially for the intralayer modes [85]. For example, the frequency of the A^2_{1g} mode in Bi_2Te_3 redshifts from 140.4 to 131.9 cm^{-1} when SOC is taken into account in the LDA calculation, which is also closer to the experimental value of 134 cm^{-1} [85].

2.4 Raman spectroscopy of 2D layered materials

The phonon properties of bulk TMDs have been studied for a long time [38, 67, 86–95]. In infrared (IR) and Raman studies, most lattice modes were observed and assigned. The conjugate pairs of A_{1g} and B_{1u} modes (~409 cm^{-1}), E^2_{1u} and E^1_{2g} modes (~384 cm^{-1}) have very similar frequencies within each pair; the frequency splitting within each pair (the so-called Davydov splitting) is related to the layer–layer (i.e., interlayer) interaction [86–88]. Later, second-order and resonant Raman spectra of MoS_2 and WS_2 provided further in-depth understanding of the lattice vibration modes [92–95]. Sugai et al. have conducted high-pressure Raman spectroscopy studies of 2H-MoS_2, 2H-$MoSe_2$, and 2H-$MoTe_2$ [90]. The pressure-dependent shifts were explained using the pressure-dependent interlayer and intralayer force constants derived from the simple linear chain model proposed by Wieting [67]. In the meantime, Raman spectroscopy studies of MS_2 (M = Mo, W) nanotubes and nanoparticles [94–96], as well as single molecular layers from chemical exfoliation [97], were reported.

Raman spectroscopy studies of lattice vibrational modes in the bulk crystal of black phosphorus can also be traced back to the 1980s [98–102]. Pressure-dependent measurements, with pressures up to 13 GPa, were conducted [98], even at low temperatures (15 K) [99]. A few modes were observed to be affected by the high pressure in terms of the frequency shift, intensity, and width. When the pressure was 1.5 GPa, the Raman frequency shifts at 15 K were found to be half of those at room temperature. Moreover, a phase transition was detected at ~5 GPa. The orthorhombic

structure (*Cmca*, D_{2h}^{18}) evolves into the rhombohedral structure ($R\bar{3}m$, D_{3d}^{6}), which can be confirmed from the fingerprint phonon modes in Raman spectroscopy [98–100]. The complete transition to the rhombohedral structure was observed to occur at ~7.7 GPa. To further the understanding, phonon dispersion curves of black phosphorus were calculated more than three decades ago, using the force constants model, but there was a large discrepancy between the calculations and experiments [101]. The investigation of phonon modes in the bulk Bi_2X_3 started even earlier, in the 1970s, using Raman spectroscopy, infrared spectroscopy, and inelastic neutron scattering [103–106].

Intensive studies on phonons in thin layers only began within the last decade. It is actually only after the resurgence of interest in graphene that the confinement effects along the vdW gap (i.e., in the out-of-plane direction) has become of concern to the community of researchers studying 2D structures, especially in the mono- to few-layer region (<10 L).

There are basically two types of Raman active modes in 2D layered materials. First, there are intralayer vibration modes, which appear in both atomically thin and bulk samples, usually at higher frequencies [45]. Second, there are interlayer vibration modes, such as the shear modes and breathing modes, where all of the atoms within each layer are displaced collectively in the same direction with the same amplitude [45, 84, 107]. The interaction within a single layer is of covalent nature, such as M–X bonding in the MX_2 layer, while the interaction between layers is mainly of the much weaker vdW type [38, 67, 86, 87], except in black phosphorus (which will be separately discussed in Section 3.3). A monolayer MX_2 has three atoms in the unit cell. Thus, a monolayer MX_2 has nine phonon modes with three acoustic branches and six optical branches at the zone center. For few-layer MX_2 (*N* layers), the number of normal phonon modes is *N* times that in a single layer. Interestingly, these new modes are derived from the single layer normal modes [84]. The situation is similar in Bi_2X_3 and black phosphorus. For example, because each layer of Bi_2X_3 has five atoms, there will be 15*N* phonon modes in *N* layers.

Lattice vibrational modes, including interlayer and intralayer modes, exhibit negligible frequency shifts as the thickness decreases from bulk to multilayer (e.g., 10 L), but layer-dependent shifts become pronounced when the thickness is further reduced from few-layer to monolayer. Such a large frequency shift has intrigued researchers, and is potentially important for applications, such as electrical and thermal conductivities, which are both affected by phonons. Besides, with reduced dimensionality and lower symmetry in thinner layers, some Raman-inactive modes in bulk and multilayer systems can become Raman-active in few-layer systems [108].

Compared with the intralayer mode, the frequency of the interlayer mode is lower (mostly < 50 cm^{-1}), much closer to the detection limit of traditional Raman spectroscopy with a single monochromator and a notch filter, which makes the observation of low-frequency modes in few-layer 2D materials challenging. The interlayer shear mode of bulk graphite located at 42 cm^{-1} was first measured by Nemanich et al. in the 1970s, using a triple grating Raman spectrometer [68]. Also using the triple grating setup, the low frequency interlayer shear mode E_{2g}^2 (33.7 ± 1 cm^{-1}) of MoS_2 was first detected by Verble et al. in 1972, and the interlayer force was found to be 100 times weaker than the intralayer force [109]. Later, interlayer shear modes in bulk $MoSe_2$ [90, 110], $MoTe_2$ [90], WS_2 [91], and WSe_2 [111] were measured. Compared with graphite, the intensity of interlayer shear modes is stronger in group VI TMDs, making the detection of such low-frequency modes possible using double monochromators [90, 93]. However, in 2D thin films, the intensity of interlayer shear modes can be much weaker and their frequencies even lower; for example, DFT calculations predicted the frequency of the interlayer shear mode in bilayer graphene to be as low as 35 cm^{-1} [112].

Most of the traditional Raman spectroscopy techniques based on the notch filter setup cannot detect such low-frequency modes in atomically thin samples owing to the strong Rayleigh scattering background. The conventional technique to reach the low frequency regime is to use the subtractive mode of a triple grating Raman spectrometer, for which the lowest detectable frequency is ~5 cm^{-1}. Recently, development of the volume Bragg notch filter has enabled the detection of low frequency modes even using a single grating Raman spectrometer. In fact, the collection

efficiency might be higher than that of the conventional triple-gating setup. By using three BragGrate filters, the interlayer shear mode of Bernal stacked few-layer graphene (FLG) was observed by Tan et al. in 2012 [113]. A blue shift in the frequency of the shear mode (C mode) was observed with increasing the film thickness. Shortly after, interlayer shear and breathing modes in few-layer TMDs were detected [84, 114–116]. Lui et al. also detected the interlayer breathing modes in FLG, and found that the frequency of the breathing mode red-shifts with increasing thickness [117, 118].

In the next section, we will discuss the recent progress in the studies of lattice vibrational modes in atomically thin 2D layered materials beyond graphene.

3 General characteristics of phonon modes in atomically thin 2D layered materials

3.1 Phonon confinement effect and electron–phonon coupling

The phonon confinement effect is a quantum size effect that occurs when the phonon wave function is confined to a small volume, with one or more dimensions of this volume having the same magnitude as the confined phonon's wavelength. In Raman spectroscopy, the direct signature of this effect is an asymmetrically broadened Raman peak that shifts toward lower frequencies in nanomaterials. In 1981, Richter et al. proposed a model to explain this effect in microcrystalline silicon (the RWL theory) [119]. Later, the RWL theory was applied to explain the nanowire diameter dependence of the asymmetric broadening and frequency shift of the one phonon (~520 cm^{-1}) band in Si nanowires [57–59]. The phonon confinement effect has also been observed in nanoparticles [94, 120]. Detailed accounts of phonon confinement in zero- and one-dimensional nanomaterials can be found in Ref. [58]. In this article, we will only provide a semi-quantitative discussion of phonon confinement in 2D layered crystals, such as Bi_2Se_3 [121].

The RWL theory [119] can be understood by considering the Heisenberg uncertainty principle: The uncertainty of the phonon momentum (Δp) and position (Δx) follows the relation $\Delta p \Delta x \geqslant \hbar/2$, with $\Delta p = \hbar \cdot \Delta k$ and Δx equal to the crystal size or thickness Δd. This indicates that phonon modes with finite non-zero momenta can be involved in Raman scattering for small Δx. Based on this principle, we can obtain the frequency shift $\Delta\omega$ if the corresponding phonon dispersion relation $\omega(k)$ is known. For example, the A_{1g}^1, A_{1g}^2, and E_g^1 modes in Bi_2Se_3 red-shift with decreasing thickness, while there is almost no difference for the E_g^2 mode. The slight red-shift in Fig. 2(b) is probably owing to a systematic error. By contrast, the red-shift is more pronounced for the A_{1g}^1 mode (Fig. 2(b)). This is in agreement with the phonon dispersion curve along the Γ–Z direction (corresponding to the direction normal to the Bi_2Se_3 layers), as only the E_g^2 mode exhibits a dispersion-less trend, as shown in Fig. 2(a). The phonon confinement effect has also been suggested to explain the shifts of the A_{1g}^1 and A_{1g}^2 modes in Bi_2Te_3 [122].

Similarly, the phonon confinement effect has been observed in monolayer MoS_2, WS_2, and WSe_2 [25, 124–126], with the lateral size (i.e., width, abbreviated as W) as a confinement variable. Figure 3(a) shows the Raman spectra of MoS_2 monolayer nanoribbons (MNRs) with different widths. The blue lines and green lines represent the zone center (Γ point) phonon modes and edge-activated modes, respectively. Due

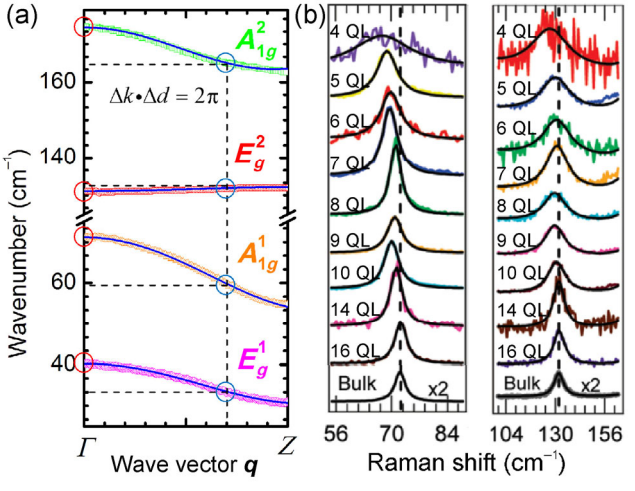

Figure 2 Phonon confinement effect in Bi_2Se_3. (a) Phonon dispersion curves of Bi_2Se_3 along the Γ–Z direction of the Brillouin zone. When the thickness (Δd) decreases, more Δk phonons are involved in the Raman scattering process, inducing peak shift and broadening. (b) and (c) Thickness-dependent A_{1g}^1 (b) and E_g^2 (c) modes. Excitation laser's wavelength is 633 nm. Reproduced with permission from Ref. [123], © American Chemical Society 2011.

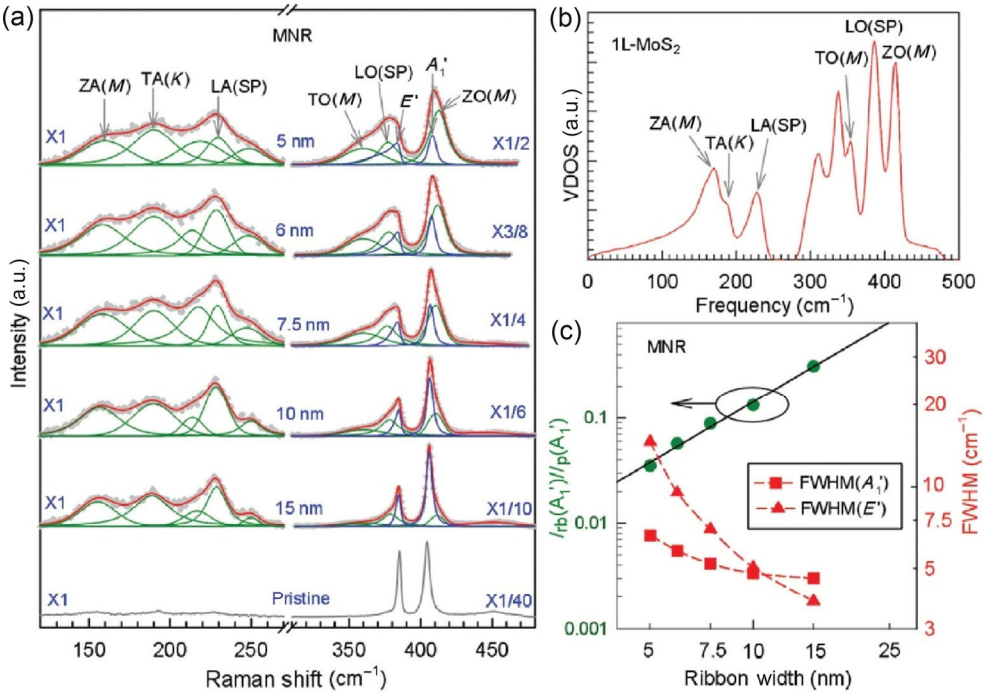

Figure 3 Phonon confinement effect in MoS_2 MNRs. (a) Raman spectra for MNRs of different widths. Experimental data are shown as the grey crosses, and the fitting results are red solid lines. The edge-activated modes and the modes (E' and A_1') broadened by the quantum confinement effect are shown as the green and blue solid lines, respectively. The Raman spectrum of pristine 1 L-MoS_2 is plotted as the grey solid line. The scaling factor of each spectrum is provided (reproduced with permission from Ref. [126], © John Wiley & Sons, Inc 2016). (b) VDOS of 1 L-MoS_2 (reproduced with permission from Ref. [127], © American Physical Society 2011). The VDOS singularities of phonon branches at the high symmetry points of the Brillouin zone are marked. (c) Peak area of the A_1' mode, $I_{rb}(A_1')$, of 1 L-MoS_2 nanoribbons normalized by that ($I_p(A_1')$) of pristine 1 L-MoS_2 with respect to the nanoribbon width, and FWHM of the E' and A_1' modes with respect to the nanoribbon width (reproduced with permission from Ref. [126], © John Wiley & Sons, Inc 2016).

to the breaking of translational symmetry, edge-activated modes appear, which can be traced to the singularities in the vibrational density of states [127] (VDOS, see Fig. 3(b)). ZA(M) denotes the ZA phonon at the M point, while LA(SP) refers to the saddle point (SP) of the LA phonon branch in Fig. 3(b).

The Γ point phonons, E' and A_1' modes, exhibit asymmetric broadening with decreasing ribbon width, as a result of the phonon confinement effect [119, 128], as shown in Figs. 3(a) and 3(c). The width-dependent line shape can be described by a Gaussian-Lorentzian profile [128]

$$I_{rb}(\omega) \propto \int \frac{\exp(-q^2W^2/2\alpha)}{[\omega-\omega(q)]^2+\Gamma_0^2}\mathrm{d}q \quad (4)$$

where $\omega(q)$ refers to the phonon dispersion, and Γ_0 is the width of the Raman mode in the bulk. When W (the ribbon width) tends to infinity, the above function approaches a Lorentzian profile, corresponding to 2D MoS_2. A width of ~40 nm is the upper limit for observing the confinement effect in 1 L MoS_2 [126].

We note that the RWL theory does not take into account the changes in frequency owing to the atomic rearrangements and/or changes in the bond strength when going from the bulk to the nanostructure. It has been shown that such effects also play an important role in explaining the frequency shifts and broadening in Si nanoparticles [129].

Here, it is important to compare the phonon confinement effect in the different materials: Bi_2X_3 (X = Se, Te), 2H-MX_2 (M = Mo, W; X = S, Se), and black phosphorus. For intralayer vibrational modes, this effect is more pronounced in Bi_2X_3 (X = Se, Te) [122, 123], as shown in the aforementioned text. Full width at half maximum (FWHM) for intralayer vibrational modes in the other two types of materials does not

exhibit appreciable thickness-dependence [130–132], except the A_{1g} mode in 2H-MX_2 (M = Mo, W; X = S, Se) [133, 134]. The linewidth of the A_{1g} mode in MoS_2 increases from 3 to 6 cm^{-1} as the thickness decreases from 6 L to 2 L, but the A_{1g} mode becomes narrower in 1 L, indicating that phonon confinement is not the only reason for the changes in linewidth [133]. The frequency shifts of the E^1_{2g} and A_{1g} modes in thin film 2H-MX_2 (M = Mo, W; X = S, Se) are also not related to the phonon confinement effect, as discussed in the next section. For interlayer vibrational modes, the frequency shift has been shown to be more related to the interlayer interaction [25, 27, 29, 84, 114–116, 135–137]. Meanwhile, the FWHM does not exhibit considerable broadening for thinner layers in Bi_2X_3 (X = Se, Te) [137], while the interlayer breathing mode becomes wider as the number of layers decreases in black phosphorus [29, 136] (this could still be related to confinement, but a detailed investigation is lacking) and 2H-MX_2 (M = Mo, W; X = S, Se) [84]. This prompts another discussion. Electron–phonon coupling and anharmonic phonon–phonon interactions are, too, believed to be crucial for determining the linewidth [113, 123, 138–140].

For instance, the A_{1g} peak of Bi_2Se_3 exhibits distinct asymmetry with the right shoulders of the peaks rising (towards high frequency). Such asymmetry has been well-captured by the Breit–Wigner–Fano (BWF) line-shape, as investigated by us for wet chemistry-synthesized Bi_2Se_3 nanoplates [123]. The BWF Raman line-shape originates from the quantum interference between a discrete phononic state and the continuum of electronic states. Constructive or destructive interferences at different frequencies result in the frequency and line-shape renormalization of a Lorentzian Raman peak

$$I(\omega) = A \cdot \frac{[q + 2(\omega - \omega_0)/W]^2}{1 + [4(\omega - \omega_0)/W]^2} \quad (5)$$

where A, ω_0, W, and q are the peak intensity, frequency, linewidth, and asymmetry parameter, respectively. The quantity $1/q$ is often used for depicting the strength of electron–phonon coupling, and when $1/q$ approaches zero the above equation reduces to a Lorentzian line-shape.

It is worth noting that the asymmetry of the peak is more distinct in thinner nanoplates, as shown by the clear contrast between 2 QL and 7 QL (Fig. 4). The thickness-dependent asymmetry is shown in Fig. 4(c), where the electron–phonon coupling strength $1/q$ monotonically increases with decreasing thickness [137]. A detailed characterization of the continuum states that are coupled with the A^1_{1g} mode and the thickness-dependent coupling strength has not been performed yet and requires further investigations. Strong electron–phonon interactions in Bi_2Se_3 have also been reported using other methods, such as the IR reflection and transmission [141, 142], ARPES [143], and electron transport measurements [144].

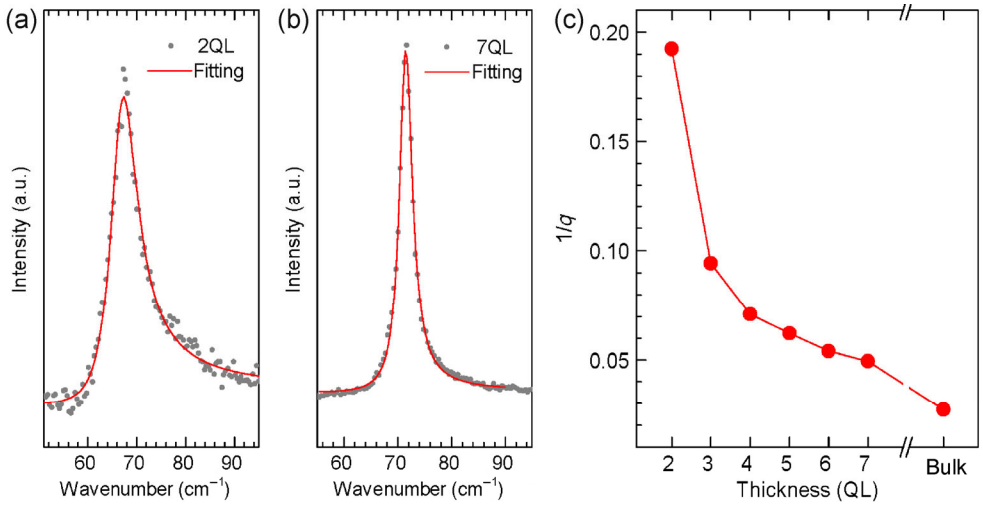

Figure 4 Fano line-shape analysis of the A^1_{1g} peak in 2–7 QL and bulk Bi_2Se_3. (a) and (b) Fano fitting for the 2 QL (a) and 7 QL (b) Bi_2Se_3. (c) The asymmetric parameter q versus the crystal thickness.

For other 2D layered materials, such as MoS_2, the influence of electron–phonon coupling and anharmonic phonon–phonon interactions on linewidth has also been demonstrated. On one hand, the thickness-dependent FWHM of the interlayer breathing mode in a few-layer MoS_2 was found to be related to the anharmonic phonon–phonon scattering [145]. On the other hand, the broadening of the A_{1g} peak has been observed when a positive gate voltage was applied to a MoS_2 monolayer. This is because a positive gate voltage introduces more electrons into the sample and increases the electron–phonon coupling, leading to the broadened linewidth [138]. In addition, recent studies have further shown that electron–phonon interaction can affect the magneto-optical Raman effect in MoS_2 [146] and anisotropic phonon behavior in black phosphorus [147].

3.2 Anomalous shifts in intralayer vibrational modes and surface effect

As discussed in Section 3.1, the frequency shift in thin film Bi_2Se_3 is consistent with the RWL theory. Here, we will discuss from a microscopic point of view other physical effects that affect the shifts in frequency as a function of thickness, focusing on the TMD materials.

With decreasing thickness, the A_{1g} mode in MoS_2 shifts toward lower frequencies (red shift, softening), while the E^1_{2g} mode shifts toward higher frequencies (blue shift, stiffening) [73, 115, 133, 148]. Figure 5(b) shows that the A_{1g} mode is softened away from the Γ point in the Γ–A direction, but the E^1_{2g} mode is dispersion-less. Therefore, a change in the frequency of the E^1_{2g} mode cannot be explained by the RWL theory. The corresponding eigenmodes are plotted in Figs. 5(c) and 5(d). In the 2 L case, the A_{1g} eigenmode corresponds to the Γ-point mode in the bulk, so that the difference between the bulk and 2 L frequencies is also not explained by the RWL theory.

Because the relative displacements of sulfur atoms in adjacent layers are out-of-phase, according to the intuitive harmonic oscillator model, the frequencies of both modes should be blue-shifted when additional layers are added, owing to the larger accumulated restoring force. This effect will be henceforth called

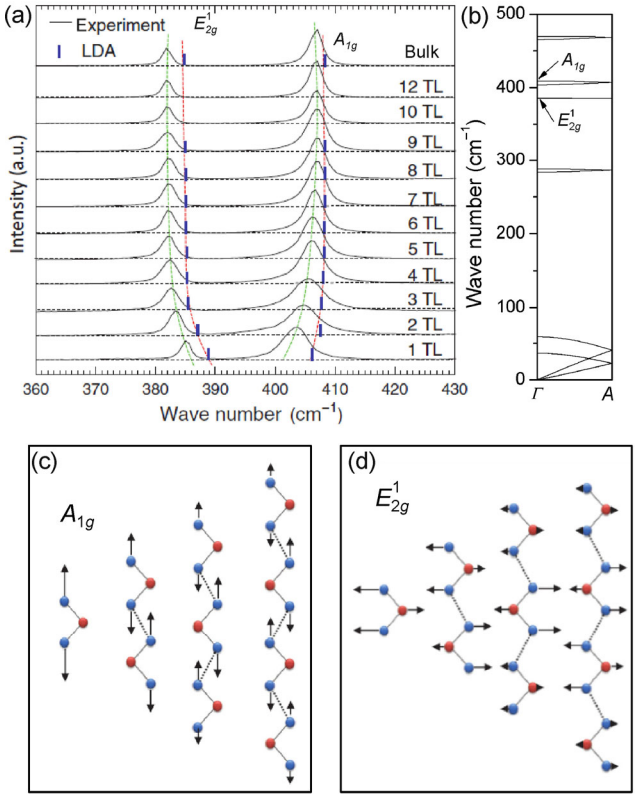

Figure 5 Raman spectra and atomic displacements of the E^1_{2g} and A_{1g} modes in mono- and few-layer MoS_2. (a) Experimental and LDA-calculated frequencies for the E^1_{2g} and A_{1g} modes in 1–12 TL and bulk MoS_2. The green and red dashed lines are used as the guides to show the trends for the experimental and LDA results, respectively. (b) Phonon dispersion of MoS_2 along the Γ–A direction. (c) and (d) Atomic displacements of the A_{1g} mode (c) and the E^1_{2g} mode (d) in 1–4 TL MoS_2. The blue and red circles represent the sulfur and molybdenum atoms, respectively. (a), (c), and (d) are adapted from Ref. [73] with permission, © American Physical Society 2013.

"the thickness effect". For the A_{1g} mode, the frequency shift is consistent with the thickness effect. On the other hand, the opposite frequency trend for the E^1_{2g} mode is not consistent with the thickness effect. The same frequency trends for the E^1_{2g} and A_{1g} modes are also observed in all of the 2H-stacked group VI TMDs, including WS_2, WSe_2, $MoSe_2$, and $MoTe_2$ [132, 134, 149–153].

Figures 6(a)–6(e) show the Raman spectra of 2H-stacked WS_2, $MoSe_2$, WSe_2, and $MoTe_2$ from bulk to few-layer, where the opposite shifts can be observed clearly. There have been conflicting conclusions regarding the assignment of the E^1_{2g} and A_{1g} modes to thin

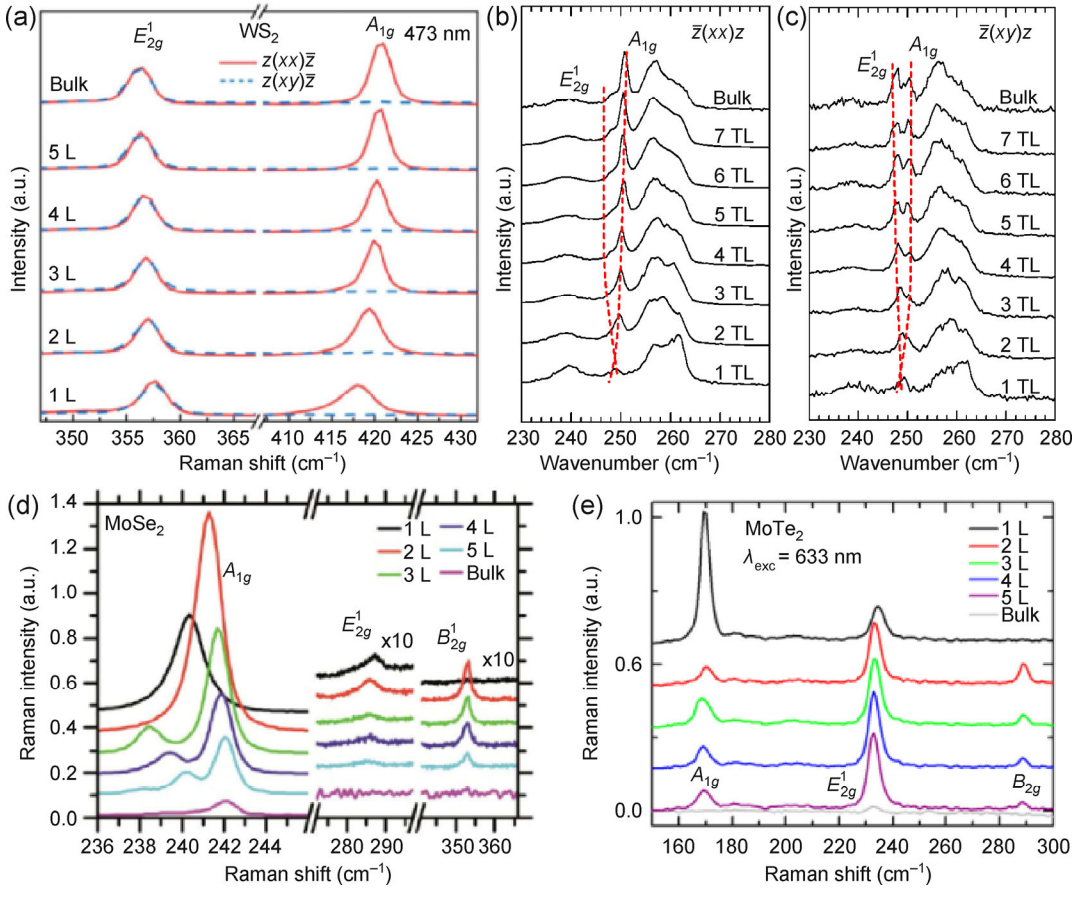

Figure 6 Raman spectra of 2H-stacked WS_2, WSe_2, $MoSe_2$, and $MoTe_2$. (a) Raman spectra of 1–5 L and bulk WS_2 in both the parallel $\bar{z}(xx)z$ and cross $\bar{z}(xy)z$ configurations (reproduced with permission from Ref. [134], © Royal Society of Chemistry 2013). (b) and (c) Raman spectra of 1–7 TL and bulk WSe_2 in the parallel $\bar{z}(xx)z$ (b) and cross $\bar{z}(xy)z$ (c) configurations. (d) and (e) Raman spectra of 1–5 L and bulk samples in $MoSe_2$ (d) (reproduced with permission from Ref. [132], © The Optical Society 2013) and in $MoTe_2$ (e) (reproduced with permission from Ref. [152], © American Chemical Society 2014).

film WSe_2 [108, 132, 134, 149, 154–156]. Theoretical calculations suggest that the E^1_{2g} and A_{1g} modes are almost degenerate in monolayer WSe_2, owing to the very close frequencies of both modes. Polarization-dependent measurements further support this conclusion, with the out-of-plane A_{1g} mode significantly suppressed in the cross-polarized $\bar{z}(xy)z$ configuration (also seen in WS_2 from Fig. 6(a)). Thus, both the E^1_{2g} and A_{1g} modes should be close to 250 cm^{-1}, as shown in Figs. 6(b) and 6(c).

Further studies were carried out to explore the anomalous frequency shifts. Here, we take 2H-MoS_2 as an example. The differences in lattice constant and interatomic distances as thickness decreases might be a possible reason for the anomalous shift, but it has been ruled out by Molina-Sanchez et al. [127]. Instead, we showed that it is the effect of larger force constants at the surface of the thin film that makes a difference to the frequency trends [157]. These larger force constants arise locally from the absence of interlayer sulphur–sulphur interactions at the surface of the thin film, and results in the anomalous blue-shift of the E^1_{2g} mode with decreasing thickness [73]. The competition between the thickness effect above and the surface effect described here will result in opposite frequency shifts of E^1_{2g} and A_{1g} modes, as observed in experiments. This frequency trend makes it convenient to determine the thickness of thin layers (< 6 L) by the frequency difference of E^1_{2g} and A_{1g} modes [133, 134]. The difference is ~19 cm^{-1} in mechanically exfoliated

monolayer MoS_2 [133]. However, a smaller value for micromechanically exfoliated monolayers (~16 cm^{-1}) [158] and larger values for laser- and thermally-thinned monolayer (> 20 cm^{-1}) were reported [159, 160]. These differing reports were mainly caused by differences in the frequency of the E^1_{2g} mode between samples. This observation further confirms the influence of surface effects, since different methods in sample preparation can possibly cause different surface environments. Even with the same method, one cannot completely avoid the problem of sample variation, as demonstrated by the mechanically exfoliated monolayer MoS_2 from Refs. [133, 158].

In the Raman community, it is widely believed that the anomalous shift of the E^1_{2g} mode in 2H-MoS_2 is related to a thickness dependence of the dielectric screening, a conclusion based on early calculations on dielectric screening by Molina-Sanchez et al. [127]. However, Lin et al. later showed experimentally that the frequencies of the E^1_{2g} and A_{1g} modes have negligible dependence on the dielectric constant of the environment [161], consistent with Ref. [73], as well as a recent review by Molina-Sanchez et al. [26].

The surface effect can also affect the frequency of the B^1_{2g} mode [108]. This mode is also observed in N layer ($N \geqslant 2$) WSe_2 even though it is not active in the bulk, owing to the lower symmetry in the thin film (see next section). Interestingly, the behavior of the B^1_{2g} mode is very similar to that of the E^1_{2g} mode in the sense that the atoms in adjacent planes are out of phase, and both modes exhibit a blue-shift with decreasing thickness. However, there are a few noteworthy differences. First, the atoms in the B^1_{2g} mode move in the out-of-plane direction (Fig. 7(a)) rather than the in-plane direction as in the E^1_{2g} mode. Second, the magnitude of the atomic displacements at the surface is larger than that in the middle for the B^1_{2g} mode (we call this a "surface mode"), in contrast to that of the E^1_{2g} mode, where the surface atoms exhibit a smaller displacement than those in the interior. As a result, the predicted frequency trend for the B^1_{2g} mode exhibits an almost constant frequency for a finite thickness (being dominated by the surface vibrations, which are thickness-independent). On the other hand, the surface effect in the E^1_{2g} mode is much larger for the mono- and bi-layer films, causing a relatively large change in the frequency when going from 3 L down to 1 L.

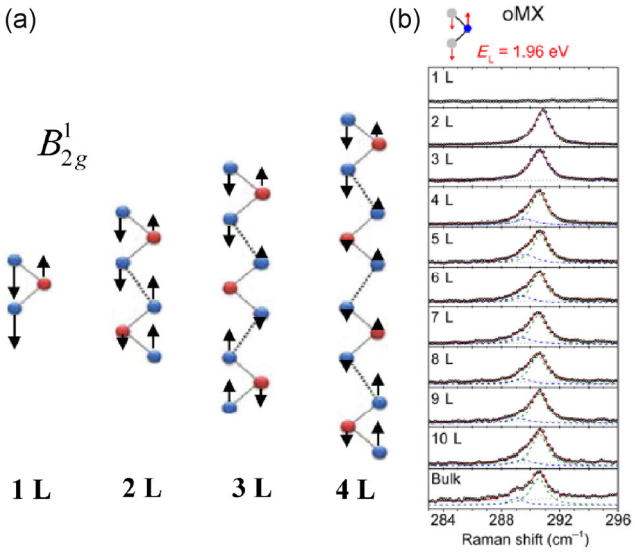

Figure 7 B^1_{2g} mode in TMDs. (a) Atomic displacement of the B^1_{2g} mode in 1–4 L TMDs (reproduced with permission from Ref. [108], © American Physical Society 2013). (b) Normalized micro-Raman spectra of the B^1_{2g} mode in N-layer $MoTe_2$. The laser photon energy E_L and the elementary intralayer displacements are indicated (reproduced with permission from Ref. [162], © American Chemical Society 2015).

The surface effect also causes the frequencies of the surface modes to be different from those of the modes involving predominantly displacements of the bulk atoms. This can explain the anomalous Davydov splitting of the out-of-plane Mo–Te mode in 2H-$MoTe_2$, as shown in Fig. 7(c) [162]. After a detailed investigation using the force constants model, Froehlicher et al. also remarked that the surface effect affects the high frequency intralayer force constants and has a negligibly influence on the interlayer modes [162].

Lastly, the Raman study of mono- and few-layer WTe_2 in the distorted orthorhombic phase has been reported recently [163]. As the layer number increases, except for the in-plane A^7_1 mode which does not shift, all the other phonon modes show a blue shift.

3.3 Reduced dimensionality and lower symmetry

In general, modes that are Raman-active in bulk are also Raman-active in thin films. However, the reverse

is not always true, owing to the lower symmetry of thin films. Reduced dimensionality and symmetry affect both intralayer and interlayer modes. Here, we will consider WSe_2 as an example, to demonstrate the effect of lower symmetry on intralayer modes [108].

The out-of-plane intralayer B^1_{2g} mode (310 cm^{-1}) and the interlayer B^2_{2g} mode (low frequency, <50 cm^{-1}, will be discussed later) are both optically inactive in bulk, but their corresponding vibration modes are Raman-active in N layer TMDs with $N \geqslant 2$, as shown in Figs. 8(a) and 8(b). According to the group theory analysis, the corresponding counterpart of the B^1_{2g} mode will evolve into the Raman-active A_{1g} mode in films with even N (311.3 and 310.1 cm^{-1} in 2 L and 4 L, respectively), while it will evolve into the Raman-active A'_1 mode in films with odd N (311.0 cm^{-1} in 3 L). This mode has A''_2 symmetry in 1 L, which is not Raman-active.

By comparison, the thickness-dependent Raman spectra of the E_{1g} mode (~176 cm^{-1}) (Figs. 8(c) and 8(d)) look similar to that of the B^1_{2g} mode (Figs. 8(a) and 8(b)), but the underlying mechanism is different. The E_{1g} mode is actually Raman-active in bulk but has zero intensity in the backscattered parallel- and cross-polarized configurations. Owing to the reduction of symmetry, the E_{1g} mode can be observed in 2–5 L WSe_2 in the parallel-polarized configuration. Note that the bulk E_{1g} mode originates from E'' in 1 L and will evolve into the Raman-active E_g in 2 L and into the E' mode in 3 L. When the thickness reaches 6 L, the mode near 176 cm^{-1} evolves into six modes, with three of them being Raman-active. The intensity of each sub-peak is only ~20% of that in 2 L WSe_2, according to our calculations. Thus, it is difficult to observe these peaks in experiments. The effects of reduced dimensionality and lower symmetry are expected to exist in all 2D TMDs. In fact, the B^1_{2g} mode has been observed in atomically thin $MoSe_2$ and $MoTe_2$, as shown in Figs. 6(d) and 6(e).

The influence of dimensionality and symmetry is more straightforward in the case of the interlayer modes. For instance, there is only one Raman-active low-frequency interlayer mode in bulk MoS_2, the shear mode E^2_{2g} (33.7 ± 1 cm^{-1}), which was detected by Verble et al. in 1972 [109]. But in few-layer MoS_2, more Raman-active interlayer shear modes can exist with different frequencies, and these modes become the degenerate E^2_{2g} mode as the thickness approaches the bulk limit. On the other hand, interlayer breathing modes are inactive in bulk, but become active and observable in few-layer systems.

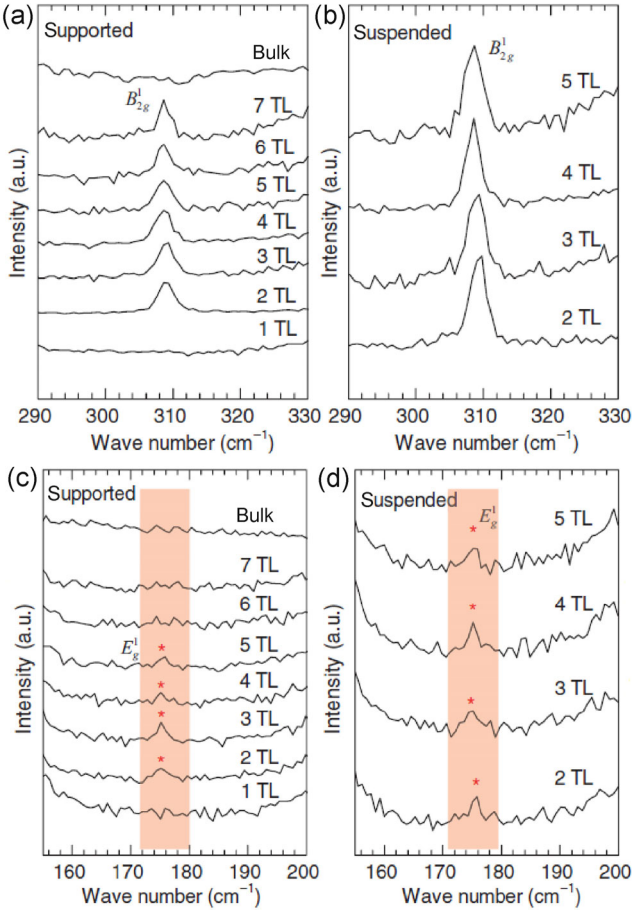

Figure 8 Raman spectra of 1–7 TL and bulk WSe_2, under 488 nm excitation. (a) Demonstration of the Raman peak at ~310 cm^{-1} in WSe_2 with SiO_2/Si substrate supported. (b) The same peak as in (a) from suspended samples. (c) and (d) The Raman peak at ~176 cm^{-1} is demonstrated in supported (c) and suspended (d) few-layer WSe_2. Reproduced with permission from Ref. [108], © American Physical Society 2013.

We first use 2H-MoS_2 and 2H-WSe_2 few-layers as examples. In N TL (N > 2) systems, there are N − 1 2-fold degenerate interlayer shear modes and N − 1 interlayer breathing modes, but not all of them can be observed from the 2H-stacked group VI TMDs. Similar to Bernal-stacked (AB-stacked) graphene, the

interlayer shear mode with the highest frequency (here labeled as the S1 mode) has the strongest intensity among all of the interlayer shear modes; meanwhile, the mode with the strongest intensity among all of the interlayer breathing modes has the lowest frequency (here this mode is labeled as the B1 mode). The S1 mode has E' symmetry in few-layer systems with odd number of layers, E_g symmetry in few-layer systems with even number of layers, and E_{2g} symmetry in bulk. The B1 mode has A_1' symmetry in few-layer systems with odd number of layers, A_{1g} symmetry in few-layer systems with even number of layers, and evolves into the optically-inactive B_{2g}^2 mode in bulk. Owing to the nature of interlayer vibrations, there are no interlayer shear and breathing modes in the monolayer.

Here E denotes the doubly degenerate in-plane modes, while A and B represent the out-of-plane vibration modes. The Raman activity of the above phonon modes can be predicted from the point group symmetry: B_{1u}, E_{2u}, and B_{2g} are optically inactive (neither Raman- nor IR-active); A_1', E'', A_{1g}, E_g, E_{1g}, and E_{2g} are Raman-active; A_2'', A_{2u}, E_u, and E_{1u} are IR-active; E' is both Raman- and IR-active. Their Raman tensors can be written as

$$A_1', A_{1g}: \begin{pmatrix} a & 0 & 0 \\ 0 & a & 0 \\ 0 & 0 & c \end{pmatrix} \quad E', E_{2g}: \begin{pmatrix} a & c & 0 \\ c & -a & 0 \\ 0 & 0 & 0 \end{pmatrix}$$

$$E'', E_{1g}: \begin{pmatrix} 0 & 0 & a \\ 0 & 0 & b \\ a & b & 0 \end{pmatrix} \quad E_g: \begin{pmatrix} a & c & d \\ c & -a & f \\ d & f & 0 \end{pmatrix}$$

Table 3 summarizes the symmetry of interlayer vibrational modes in few-layer and bulk MoS_2/WSe_2.

Figure 9 shows the low-frequency Raman spectra of 1–12 L and bulk MoS_2 and WSe_2. Except the S1 and B1 modes, other interlayer vibration modes, labeled S2 and B2, are also observed. The S2 and B2 modes are the 3rd highest frequency interlayer shear mode and the 3rd lowest frequency interlayer breathing mode, respectively. They only show up when N is larger than four, with the corresponding atomic displacement shown in Figs. 10(b) and 10(c). Meanwhile, the S2 and B2 modes have much lower intensity compared with the S1 and B1 modes, which is in agreement with the theoretical calculations. The 2nd highest frequency

Table 3 Interlayer vibrational modes in bulk and few-TL MoS_2/WSe_2[a]

Sample	Interlayer shear modes		Interlayer breathing modes	
Bulk	E_{2g}^2 (R)		B_{2g}^2 (inactive)	
N TL (N odd)	E' (I+R)	E'' (R)	A'_1 (R)	A''_2 (I)
N TL (N even)	E_g (R)	E_u (I)	A_{1g} (R)	A_{2u} (I)

[a] R and I refer to Raman- and IR-active modes, respectively. Reproduced with permission from Ref. [84], © American Chemical Society 2013.

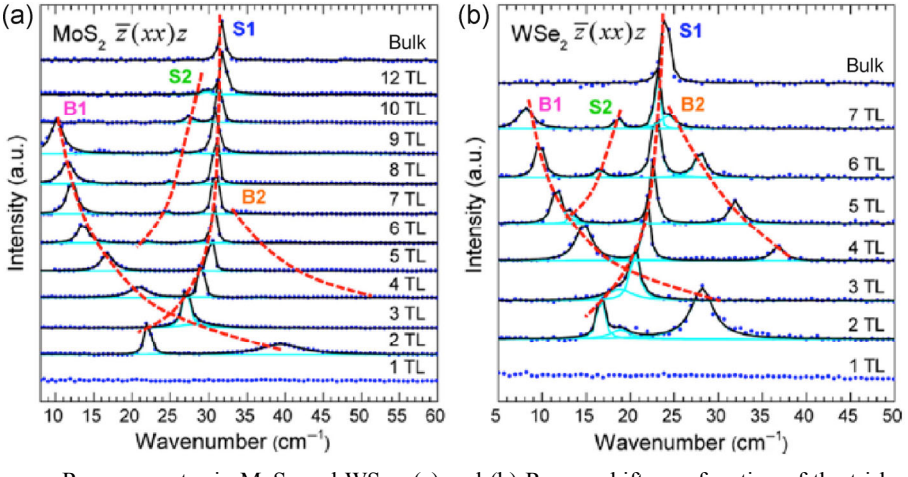

Figure 9 Low-frequency Raman spectra in MoS_2 and WSe_2. (a) and (b) Raman shift as a function of the tri-layer number, for MoS_2 (a) and WSe_2 (b), measured using the $\bar{z}(xx)z$ configuration. The blue dots are the experimental data points, while the black solid curves are the Lorentzian fits to the data. The Rayleigh scattering background has been subtracted for all of the spectra using a polynomial baseline treatment. Reproduced with permission from Ref. [84], © American Chemical Society 2013.

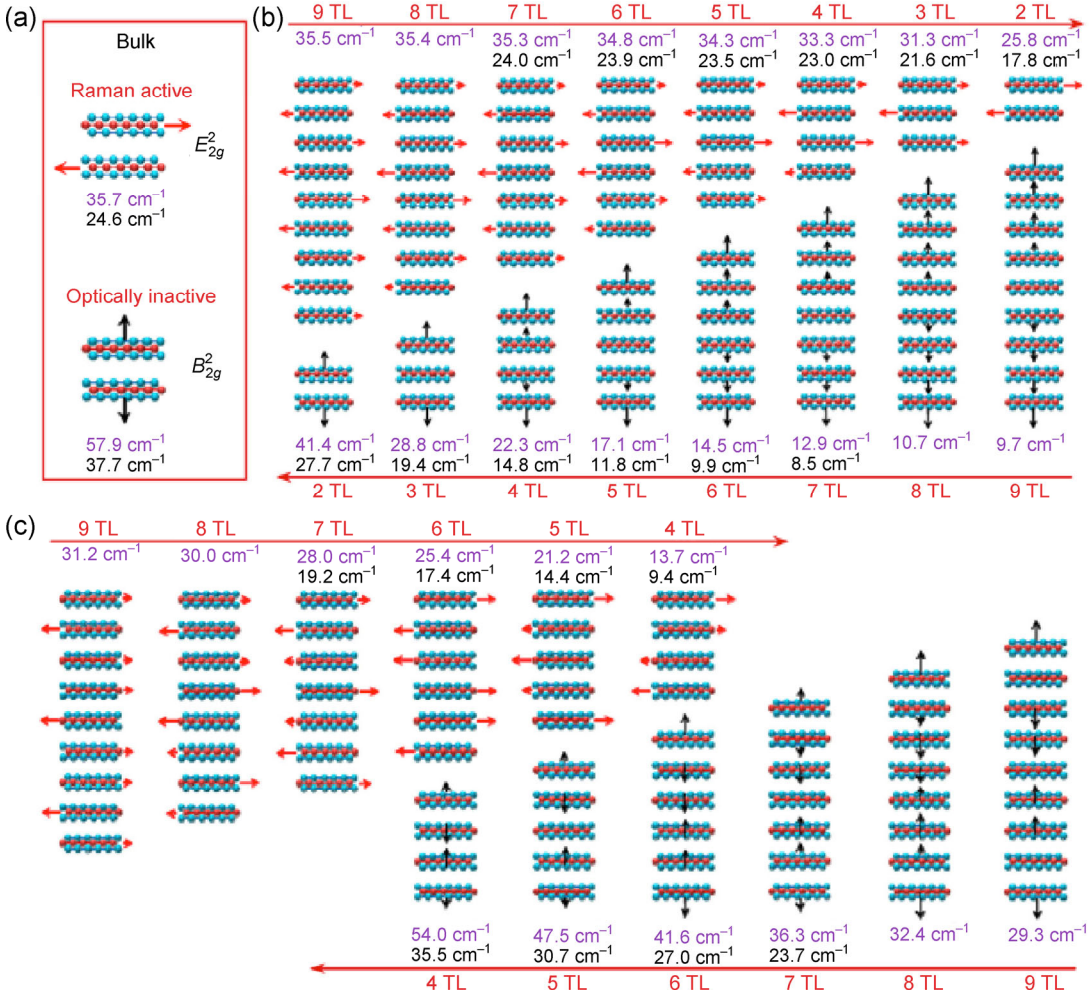

Figure 10 Atomic displacements of the interlayer shear and breathing modes in MoS_2 and WSe_2. (a) Interlayer shear and breathing modes in bulk. (b) Vibrational normal modes of the highest frequency shear mode and the lowest frequency breathing mode from 2–9 L. (c) Vibrational normal modes of the third highest frequency shear mode and the third lowest frequency breathing mode from 4–9 L. Reproduced with permission from Ref. [84], © American Chemical Society 2013.

shear mode and the 2nd lowest frequency breathing mode cannot be observed from spectra, but the reasons for this differ for films with odd/even number of layers: The two modes are Raman-inactive modes for even N (2 L, 4 L …). In contrast, they are Raman-active modes for odd N (3 L, 5 L …), but the corresponding Raman cross-sections are zero in the backscattering configuration, a commonly used setup for micro-Raman spectroscopy.

The topologically insulating Bi_2X_3 (X = Se, Te) few-layer systems also exhibit low-frequency interlayer shear and breathing modes. As shown in Fig. 11, many low-frequency Raman peaks are observed. Two trends are particularly prominent, both showing blue-shifts with decreasing thickness, as guided by the blue and red dashed lines. They are the lowest frequency interlayer breathing mode B1 (blue) and the lowest frequency interlayer shear mode S1 (red), respectively.

We make a comparison between Bi_2X_3 (X = Se, Te) and 2H-MX_2 (M = Mo, W; X = S, Se, Te) in the low frequency region by taking Bi_2Te_3 and 2H-MoS_2 as representatives. There are two main differences: (1) In bulk Bi_2Te_3, interlayer vibrational modes are excluded in the irreducible representations of the Γ phonon modes under its rhombohedral structure; (2) while the frequency trends for the observed interlayer breathing modes are the same in both materials, the observed interlayer shear modes blue-shift with decreasing

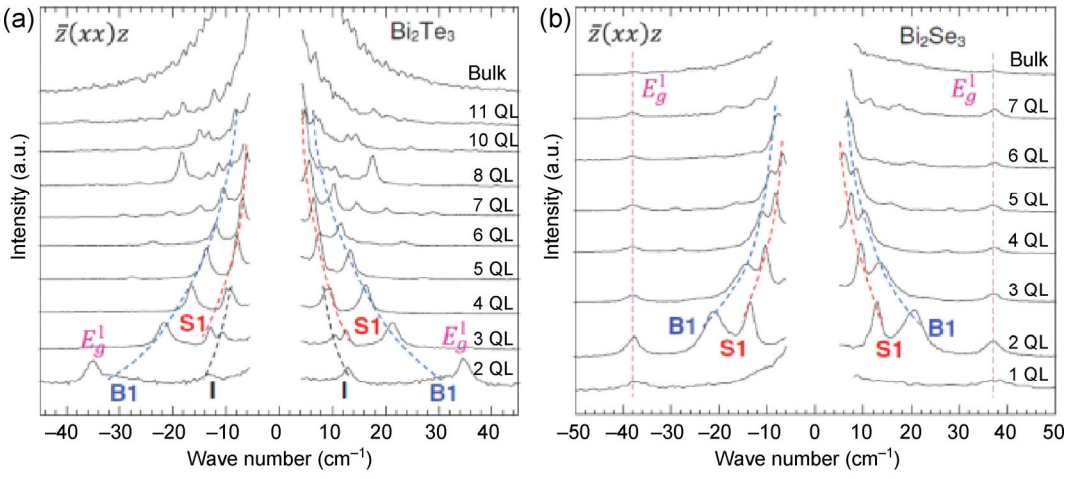

Figure 11 Interlayer vibrational modes in Bi_2X_3 (X = Se, Te). (a) and (b) Low-frequency Raman spectra, as a function of the number of layers in Bi_2Te_3 (a) and Bi_2Se_3 (b), measured using the $\bar{z}(xx)z$ configuration. The lowest frequency interlayer breathing, shear modes, and the out-of-plane interface phonon modes are denoted as B1, S1, and I, respectively, and their trends are guided by the blue, red, and black dashed lines. The interface mode (I mode) will be discussed in Section 3.4. Reproduced with permission from Ref. [137], © American Physical Society 2014.

thickness for Bi_2Te_3 and red-shift with decreasing thickness for 2H-MoS_2.

To further confirm that interlayer vibrational modes are universal in 2D layered materials, here we show the low-frequency Raman spectra of black phosphorus in Fig. 12. The A_g^3 mode, which is the interlayer breathing mode with the lowest frequency, exhibits a larger thickness-dependent frequency change compared with other 2D layered materials. The A_g^3 mode shifts from ~39 cm^{-1} in 4 L to ~16 cm^{-1} in 10 L from the spectra. This thickness dependence is significantly larger than that in TMDs such as MoS_2. (The B1 mode in MoS_2 shifts from ~21 cm^{-1} in 4 L to ~12 cm^{-1} in 9 L.) From these frequency shifts, we can extract the effective force constants between layers using the linear chain force constants model (described in the next section). The derived out-of-plane force constant is 14.1 × 10^{19} N·m^{-3}, which is ~50% larger than that for graphite and MoS_2 (see Table 4 in Section 3.4 for more details).

These large force constants are indicative of unusually large interlayer interactions in black phosphorus compared with other layered materials [29]. It was found that DFT LDA and vdW-DF2-c09 (vdW-DF2 with Cooper's exchange) both yield a significant covalent interaction between layers. Later, high-level quantum Monte Carlo (QMC) calculations showed that the interlayer interaction between phosphorene layers is in fact owing to a redistribution of electron charge from the interlayer region to the intralayer region (Fig. 12(b)), while LDA and most vdW functionals yield a covalent interaction [164].

In Fig. 12(a), two modes are apparent between 80 and 90 cm^{-1}. These are not interlayer shear or breathing modes, as these modes all red-shift with increasing thickness, while the experimentally observed modes blue-shift with increasing thickness.

3.4 Linear chain model and substrate effect

We have shown in the previous section that interlayer vibrational modes are common in 2D layered materials, especially in few-layer systems. In this and the next section, we will discuss a few interesting and general questions related to the observed interlayer modes. What determines the thickness dependence of Raman shifts? Why are these trends different for the observed interlayer shear modes in different materials? What can be said about the interaction between the sample and the substrate?

Back in 1973, the lattice vibrations of MoS_2 were interpreted using a linear chain model that was proposed by Wieting [67]. In 1982, the pressure-dependent interlayer and intralayer force constants of MoS_2 were obtained, also using the linear chain model [90]. In 1996, the linear chain model was further

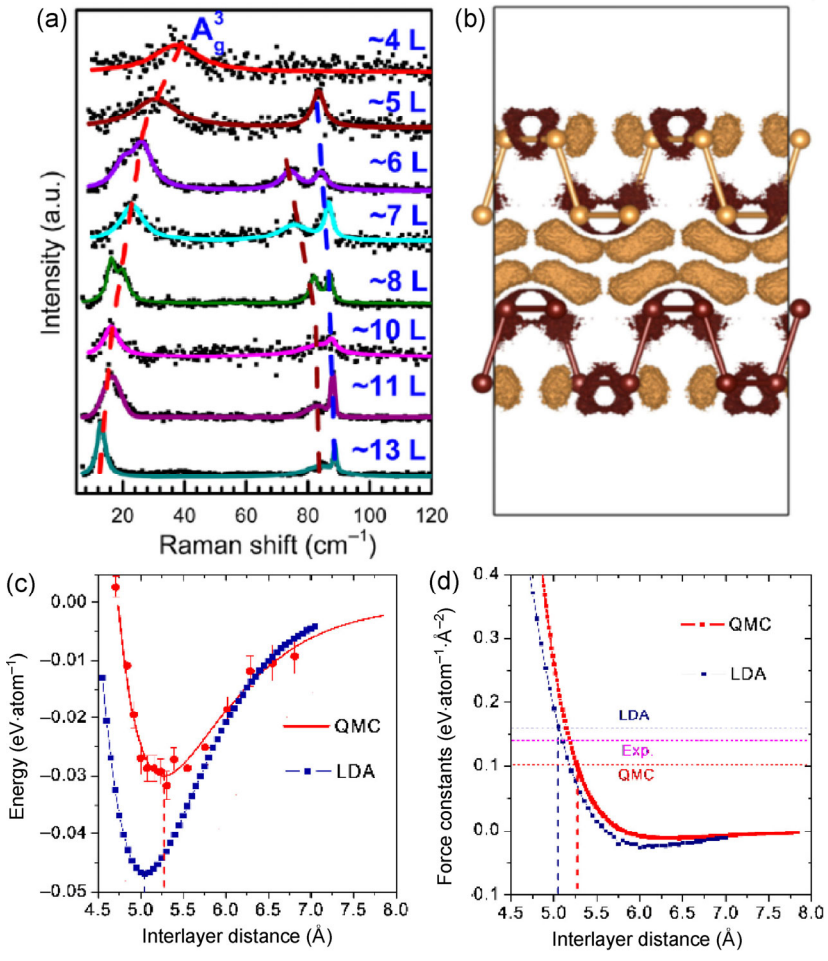

Figure 12 Interlayer vibrational modes in the few-layer black phosphorus. (a) Low-frequency Raman spectra of black phosphorus measured in the backscattering configuration for the range of 10–120 cm^{-1} (reproduced with permission from Ref. [29], © American Chemical Society 2015). (b) Electron density differences for AB-stacked black phosphorus bilayers, with the excess electron density shown in dark brown and the electron deficiency shown in light brown (reproduced with permission from Ref. [164], © American Chemical Society 2015). (c) and (d) Quantum Monte Carlo [164] and LDA-calculated binding energy (c) and derived force constants (d), versus the interlayer distance. The vertical dashed lines indicate the equilibria for the two calculations, while the force constants in the experiment are derived from the Raman frequencies in Ref. [29].

used to explain the breathing mode in epitaxial thin films [165].

We discuss the linear chain model in the context of interlayer phonon modes in layered materials. The linear chain model is a simple model in which the lattice vibrations are related to the interlayer interaction, as well as to the coupling between the sample and the substrate (with the force constant denoted by K_i in Fig. 13(a)). In general, this model only considers the interlayer coupling between adjacent layers [84, 113]. Within the N-layer sample as shown in Fig. 13(a), K_z and K_x refer to the out-of-plane and in-plane force constants, respectively. Figure 13(b) shows schematically the layer displacements that are obtained for interlayer modes when this model is applied to 2 L Bi_2Te_3 grown by chemical vapor deposition (CVD) on a SiO_2/Si substrate [166].

In CVD-grown few-layer Bi_2Te_3 on SiO_2/Si [166], the substrate effect (here referring to the interaction between the sample and the substrate) on the interlayer mode frequencies cannot be neglected (Figs. 11(a) and 13(c)). However, Raman spectra of substrate-supported and suspended few-layered MoS_2 (and WSe_2) show almost no difference, indicating that the interaction between the substrate and sample in these systems is negligible [84, 108].

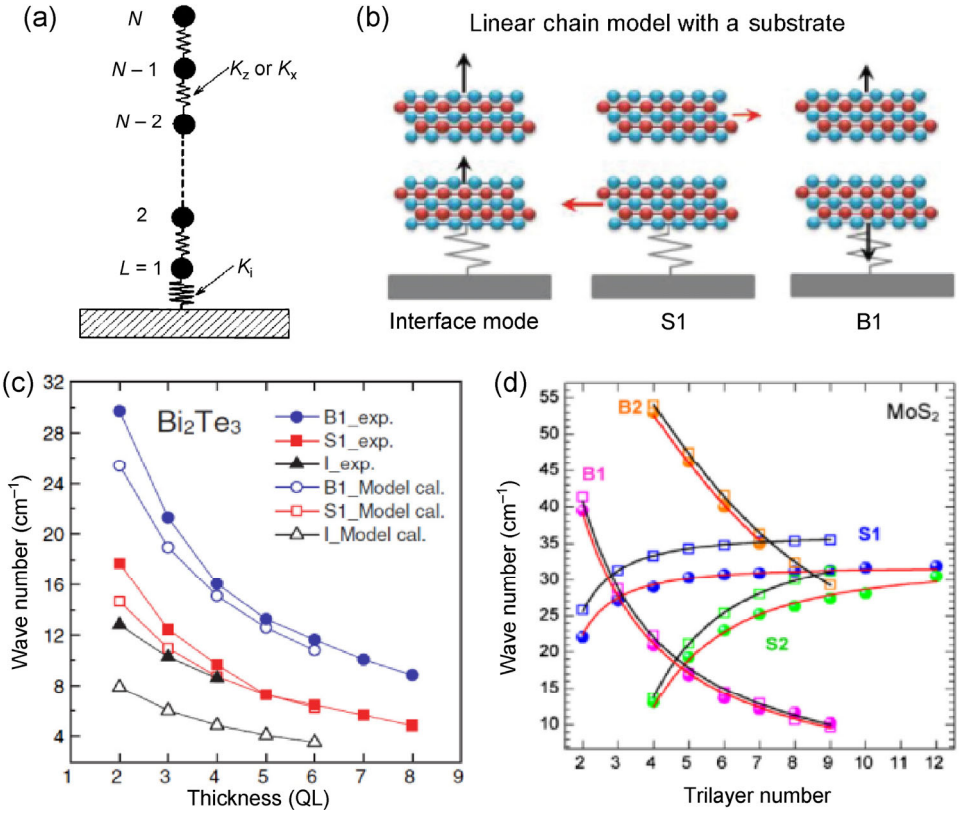

Figure 13 Linear chain model and frequency trends of interlayer vibrational modes. (a) Schematic of the linear chain model of an N-layer sample with a substrate. One sphere corresponds to one layer. K_z (K_x) refers to the out-of-plane (in-plane) force constant between adjacent layers. K_i denotes the interaction between the sample and the substrate. (b) Displacement schematics of the interface (I mode), S1, and B1 modes in 2 L Bi_2Te_3, in the linear chain model with a substrate. The arrows indicate the vibration directions, and their lengths are proportional to the displacement amplitudes. (c) Comparison between the experimental and the DFT-calculated frequencies for the S1, B1, and I modes, in the linear chain model with a substrate interaction (K_i/K = 0.5) in few-layer Bi_2Te_3. (d) Frequencies of shear and breathing modes as a function of the number of layers in MoS_2. Experimental data in (c) and (d) are shown with solid dots/squares/triangles, while open ones represent the DFT calculation results. (a), (b), (c), and (d) are adapted with permission from Ref. [165] (© American Physical Society 1996), Ref. [137] (© American Physical Society 2014), and Ref. [84] (© American Chemical Society 2013), respectively.

Within the linear chain model, the phonon frequencies (units: cm^{-1}) are given by

$$\omega_\alpha = \sqrt{\frac{K}{2\mu\pi^2 c^2}\left(1-\cos\left(\frac{(\alpha-1)\pi}{N}\right)\right)} \quad (6)$$

with N denoting the number of layers and K denoting the force constant per unit area. Without considering the substrate effect (i.e., with K_i = 0 N·m^{-3}), K corresponds to K_z and K_x for breathing modes and shear modes, respectively. The parameter μ is the mass per unit area (e.g., μ = 8.2×10^{-6} kg·m^{-2} for Bi_2Te_3, μ = 3.1 × 10^{-6} kg·m^{-2} for MoS_2), and c is the speed of light. The setting α = 1 corresponds to the acoustic mode. In 2H-MoS_2 and WSe_2, $\alpha = N$, (N – 2), 2, 4 correspond respectively to S1, S2, B1, and B2, described above. In Bi_2Te_3 and Bi_2Se_3, α = 2 corresponds to both S1 and B1. From Figs. 13(c) and 13(d), we see that the linear chain model provides a good fit to the experimental and DFT-calculated frequency trends. From these fits, the corresponding force constants are obtained and listed in Table 4. Remarkably, we note that as $N \to \infty$, the linear chain model with K_x extracted from the thin film frequencies predicts bulk S1 frequencies in a very good agreement with the actual calculated/measured values (listed in Table 4).

A non-zero force constant K_i, describing the interaction between the substrate and the film's bottom

Table 4 Force constants per unit area derived from the linear chain model fits, and the corresponding predicted S1 frequencies in the bulk. The numbers in this table are obtained from Refs. [84] (TMD materials), [137] (Bi_2Te_3 and Bi_2Se_3), and [29] (black phosphorus)

Sample	Parameter	DFT (LDA)	Experiment
MoS_2	K_z (10^{19} N·m^{-3})	9.26	8.62
	K_x (10^{19} N·m^{-3})	3.51	2.72
	Bulk S1 frequency (cm^{-1})	36.1[a] (35.7)	31.8[a] (31.7)
WSe_2	K_z (10^{19} N·m^{-3})	8.38	8.63
	K_x (10^{19} N·m^{-3})	3.41	3.07
	Bulk S1 frequency (cm^{-1})	24.8[a] (24.6)	23.5[a] (24.0)
Bi_2Te_3	K_z (10^{19} N·m^{-3})	8.21	13.33[b]
	K_x (10^{19} N·m^{-3})	2.76	4.57
Bi_2Se_3	K_z (10^{19} N·m^{-3})	6.34	5.26
	K_x (10^{19} N·m^{-3})	3.10	2.27
Black phosphorus	K_z (10^{19} N·m^{-3})	14.1	12.7

[a]Values predicted by the linear chain model, while the values in parentheses were calculated explicitly using DFT (left column) or were experimentally measured (right column) for the bulk material.
[b]The substrate effect has been accounted for in deriving this value.

layer, was required to explain the low frequency I mode (see Fig. 11) in CVD-grown Bi_2Te_3 nanoplates on SiO_2/Si. This nonzero K_i results in an interfacial mode (I mode; Fig. 13(b)) with a finite frequency. The calculated results in Fig. 13(c) were obtained using the linear chain model with $K_i/K_z = 0.5$. The frequency trend agrees with the experimental observations. Figure 14 shows the low frequency Raman spectra of 2 L and 3 L Bi_2Te_3, for different substrates. The spectra were carefully analyzed using multi-Lorentzian fitting superimposed on a polynomial background. The B1 and S1 peaks barely show any substrate dependence, similar to those in 2H-MoS_2. The I peak, however, is relatively more sensitive to the substrate, supporting its origin as a substrate-introduced I mode [137]. From our calculations, the B1 and S1 frequencies also change slightly when K_i/K_z changes. However, the frequency change for the I mode is much larger than those for the B1 and S1 modes when $K_i/K_z < 1$ [137]. By comparison, there is no I mode in MoS_2, but it has been shown that the substrate affects the Raman intensity due to interference effects [167].

The linear chain model has also been applied to analyze the interlayer modes observed in multilayer graphene and black phosphorus [113]. As we have discussed in Section 3.3, the interlayer out-of-plane force constant is significantly larger in black phosphorus (Table 4). Earlier, we had commented that DFT LDA works very well for predicting both interlayer and intralayer phonon frequencies in layered materials. This is also evident from Table 4, in which the LDA-derived force constants are in a good agreement with the experimental ones. However, we also saw that for black phosphorus, DFT LDA predicts qualitatively different interlayer interactions, based on more accurate QMC calculations. Here, we also extracted the out-of-plane interlayer force constant of black phosphorus from the QMC potential energy surface calculations, and compared these calculated values with the experimental and LDA-derived values (Figs. 12(c) and 12(d)). The LDA force constants derived in this manner match well with those obtained from the above-described fits of the linear chain model, overestimating the experimental force constant by ~14%. The QMC-derived force constant underestimates the experimental force constant by 28%. It is unknown at present why QMC cannot predict the force constant as well as DFT LDA. Possible factors include the Morse potential fitting required for QMC, as well as the possibility that adsorbates or substrate effects affect the experimentally measured force constant in black phosphorus.

In addition, the linear chain model has been adopted to describe the interlayer breathing mode of a bilayer heterostructure (based on 1 L MoS_2 and 1 L $MoSe_2$ (WSe_2)) [168]. The excellent fits of the linear chain model to experimental data and to first principles calculations clearly indicate that the interlayer phonon eigenmodes can be described by effective interlayer interactions involving nearest neighbors in most situations.

Next nearest neighbors have been considered by Wang et al. [169] and Wu et al. [170]. For example, the frequencies of the interlayer breathing modes in twisted multilayer graphene are underestimated by a linear chain model considering nearest neighbors

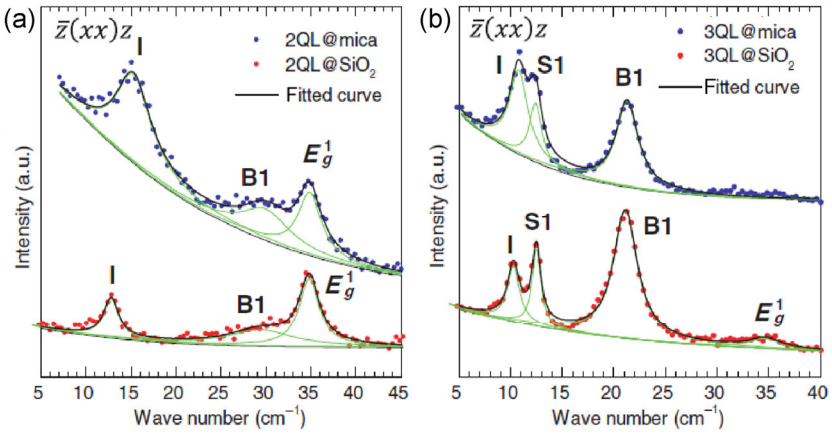

Figure 14 Substrate-dependent Raman spectra of few-layer Bi_2Te_3 nanoplates. (a) and (b) Spectra taken on 2 L (a) and 3 L (b). Data from mica and SiO_2 are shown as the blue dots and red dots, respectively. Reproduced with permission from Ref. [137], © American Physical Society 2014.

only. When next nearest neighbors are included as well, an excellent agreement between experiments and the linear chain model can be reached [170].

3.5 Stacking orders and interlayer shear modes

By comparing the frequency trends of the interlayer vibrational modes in 2H-stacked TMDs and ABC-stacked Bi_2X_3 (X = Te, Se) few-layers [84, 137], we have found that in both systems the breathing modes exhibit the same trends (i.e., red-shifts in thicker samples), while the shear modes behave differently: As the thickness increases, the shear modes blue-shift in 2H-TMDs, but red-shift in Bi_2X_3 (X = Te, Se).

As discussed above, the symmetry or space group can determine the Raman activity of phonon modes. However, in the low frequency region, a trend is determined by the Raman-active modes with the largest Raman intensity. It is interesting to ask what determines the direction of this trend. In other words, is there any general rule that determines the largest Raman intensity of the interlayer modes?

We note that the 2H TMD is AB-stacked, while the rhombohedral Bi_2X_3 is in the ABC stacking order. Both the AB and ABC stacking orders can occur stably in graphite and TMD materials with different space groups and symmetries. Research on the effects of different stacking orders has led to interesting discoveries. Let us consider MoS_2 as an example. The commonly seen 2H-MoS_2 is centrosymmetric in the bulk. In thin layers, the crystal structure is non-centrosymmetric in films with an odd number of layers (1 L, 3 L, …) and centrosymmetric otherwise (2 L, 4 L, …); this can be experimentally probed from layer-dependent second harmonic generation [171]. In contrast, the 3R-MoS_2 crystal is centrosymmetric from monolayer to bulk. Thus, strong valley polarization was observed in the bilayer 3R-MoS_2 using photoluminescence spectroscopy [39]; while there is almost no valley polarization in the bilayer 2H-MoS_2 (the small polarization is probably related to the substrate) [22, 23, 39]. 1T-MoS_2 is another polytype. Different from the semiconducting 3R and 2H phases, 1T-MoS_2 is metallic (distorted forms of 1T phases have a small band gap) and can be used as the electrode, which can help to improve device performance in MoS_2 by reducing the contact resistance [172].

Studies on other more complex stacking configurations (e.g., ABCB stacking in 4 L TMDs) and samples with twist (stacking) angle have also intrigued many researchers [173–177]. Moreover, the stacking angle is further shown to affect the optical properties of heterostructures [168, 178, 179]. In this section, we will focus on the effect of the stacking order on the interlayer modes; where by stating stacking order, we refer to traditional way of defining AB and ABC stacking sequences, which was also discussed in the preceding paragraph [38]. Considering the importance of the stacking order, developing a rapid way to identify the phase is crucial. Generally, we find that the stacking order does not significantly change the

interlayer frequency. However, the stacking order affects the Raman intensity of the interlayer shear modes [151, 180, 181]. At the end of this section, we will discuss the effect of the twist (stacking) angle, which significantly affects both the frequency and Raman intensity of the interlayer vibrational modes [182, 183].

Because Raman activity is determined by the material's space group and symmetry, it is important to first discuss the symmetry of different material polytypes. The space groups (symmetries) of multi-layered graphene, MoS_2 (TMDs), and Bi_2Se_3 (Bi_2Te_3) are listed in Table 1, for different numbers of layers and different stacking orders. It is clear that the space group (symmetry) does not explain the Raman intensities of the interlayer shear modes. For example, both AB (Bernal) and ABC stacked four-layer graphene (4 LG) have the same symmetry (D^3_{3d}), even though the highest frequency interlayer shear mode (C mode) has a large Raman intensity in AB-stacked 4 LG [113] but a negligible Raman intensity in ABC-stacked 4 LG [184]. Likewise, for films with an even number of layers, ABC-stacked Bi_2Se_3 and Bi_2Te_3 have the same space group (D^3_{3d}) as AB- and ABC-stacked graphene, but the frequency trend of ABC-stacked Bi_2Se_3 and Bi_2Te_3 is the same as that of ABC-stacked graphene, instead of AB-stacked graphene. On the other hand, although ABC-stacked graphene (D^3_{3d}) and ABC-stacked (3R phase) MoS_2 and $MoSe_2$ (C^1_{3v}) have different symmetries, their interlayer shear modes exhibit the same frequency trends in the Raman spectra (red-shifts in thicker samples). Therefore, it seems that the stacking order, rather than the space group, affects the observed Raman spectral trends in the interlayer shear modes.

The observed frequency trends depend on which of the interlayer shear modes has the largest Raman intensity. For AB-stacked materials, the highest frequency shear mode (maximal out-of-phase displacements in adjacent layers) has the largest Raman intensity, while for ABC-stacked materials, the lowest frequency shear mode (minimal out-of-phase displacements in adjacent layers) has the largest Raman intensity. These observations would seem consistent with the physical intuition that a maximal out-of-phase displacement would result in the largest change in polarizability (and therefore the largest Raman intensity) in AB-stacked materials, while the opposite is true for ABC-stacked materials. This physical intuition can be confirmed more quantitatively using the bond polarizability model [184]. As shown in Section 2.3, the non-resonant Raman intensity can be calculated using the derivative of the electronic polarizability in the Placzek approximation. Within the bond polarizability model, the electronic polarizability is written as a sum of individual bond polarizabilities, which are assumed to be roughly independent of the chemical environment [185]

$$P_{\alpha\beta}=\frac{1}{2}\sum_{l,B}\left\{\frac{1}{3}\left(\alpha_{||}+2\alpha_{\perp}\right)\delta_{\alpha\beta}+\left(\alpha_{||}-\alpha_{\perp}\right)\left(R_{\alpha}R_{\beta}-\frac{1}{3}\delta_{\alpha\beta}\right)\right\} \tag{7}$$

where $\boldsymbol{R}\equiv\boldsymbol{R}(l,B)$ is the bond vector connecting the atom l to one of its nearest neighbors l' connected by the bond B, the vector being normalized to unity. The parameters $\alpha_{||}$ and $\alpha_{\perp}$ are the static longitudinal and perpendicular bond polarizabilities, respectively, which are further assumed to depend only on the bond length R. The derivative of the bond polarizability in the $\bar{z}(xx)z$ configuration, which determines the Raman intensity in most of our measurements, can be written as

$$P_{xx,k}=-\sum_{lB}\left\{\frac{\alpha'_{||}+2\alpha'_{\perp}}{3}\vec{R}_0\cdot\vec{\chi}^k_l+(\alpha'_{||}-\alpha'_{\perp})R^2_{0x}\vec{R}_0\cdot\vec{\chi}^k_l-\right.$$
$$\left.\frac{1}{3}(\alpha'_{||}-\alpha'_{\perp})\vec{R}_0\cdot\vec{\chi}^k_l+2R_{0x}\chi^k_{lx}\frac{\alpha_{||}-\alpha_{\perp}}{R_0}-2\frac{\alpha_{||}-\alpha_{\perp}}{R_0}R^2_{0x}\vec{R}_0\cdot\vec{\chi}^k_l\right\} \tag{8}$$

where $\vec{R}_0$ is the bond vector at equilibrium, normalized to unity, R_0 is the bond length at equilibrium, R_{0x} is the x component of $\vec{R}_0$, the "primes" on the polarizabilities refer to the radial derivatives with respect to the atomic displacements, and χ^k_l is the eigenvector of the phonon mode k.

Using the bond polarizabilty model, we observe that the Raman intensity in the $\bar{z}(xx)z$ configuration is zero for the lowest frequency interlayer shear mode and largest for the highest frequency interlayer shear mode in AB-stacked systems, while the opposite is true for ABC-stacked systems (see Fig. 15(b) for an example in 3 L graphene) [184]. These different Raman intensities determine the frequency trends observed in Raman spectra.

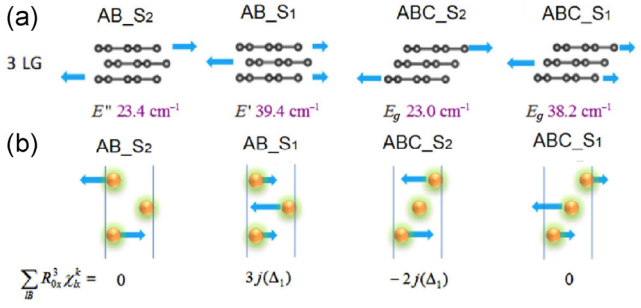

Figure 15 Stacking orders and interlayer shear modes. (a) Atomic displacements of the interlayer shear modes in AB and ABC stacked 3 LG. (b) General bond polarizability model in AB and ABC stacked 3 LG. The sphere represents a graphene layer. As there are only two interlayer shear modes in 3 LG, the higher-frequency peak is denoted S1, while the other peak is denoted S2. Reproduced with permission from Ref. [184], © Nature Publishing Group 2015.

The influence of the stacking order on the Raman intensity of the interlayer shear modes is general for all 2D layered materials, i.e., the frequency of the interlayer shear modes red-shifts in ABC stacked systems and blue-shifts in AB stacked systems with increasing the film thickness. In contrast, the in-plane stacking difference will not affect the polarizability in the *z* direction, thus not affecting the frequency trend of the breathing mode.

As a direct advantage of using the bond polarizability model as well as DFT calculations, various stacking sequences can be determined readily by using the interlayer shear modes. Here, we consider CVD-grown $MoSe_2$ flakes [151, 182, 186] with multiple stacking combinations as an example for further analysis. In Section 3.3, we have mentioned that it is not always possible to observe all of the $N - 1$ interlayer shear modes in an N layer system. For brevity, we refer to the interlayer shear modes as S_1, S_2, S_3, …, starting from the highest frequency and advancing in the order of decreasing frequency. In 2H stacking, counting from the highest frequency, only the odd interlayer shear modes (S_1, S_3, S_5, …) are observable. Moreover, the peak intensity of all the observable interlayer shear modes in 2H exhibits the trend $I(S_1) > I(S_3) > I(S_5) >$ … relative to each other, as shown in the experimental spectra in Fig. 16(a). In contrast, the relative peak intensity in 3R stacking exhibits the trend opposite to that of 2H stacking, with the lowest frequency mode (S_{N-1}) having the highest intensity [151].

From the above analysis, we see that by identifying the frequencies of active modes (2H-3 L: ~23 cm^{-1}; 3R-3 L: ~13 cm^{-1}) or comparing the relative intensities (2H-4 L: $I(S_1) > I(S_3)$; 3R-4 L: $I(S_3) > I(S_1)$), stacking sequences can be determined rapidly. However, it is challenging to identify stacking in 2 L in terms of the peak position and relative intensity, because the bilayer only has the S_1 mode (Fig. 16(d)). Puretzky et al. show that the absolute intensities of the S_1 modes in 2H- and 3R-stacked bilayer $MoSe_2$ are very different, as shown in Fig. 16(c) [180].

Other than the 2H and 3R phases, stacking faults, such as ABCB stacking in 4 L, can also be identified using the bond polarizability model. In 4 L $MoSe_2$, neither 2H (ABAB) nor 3R (ABCA) stacking can give rise to a strong S_2 mode. The bond polarizability model and DFT calculations showed that it is a stacking fault that leads to the appearance of this mode. Other combinations, such as mixtures of 2H and 3R, are also assigned in 3–5 L. A mixture can be either in-plane (in the *xy* plane) owing to the co-existence of samples with different stacking orders, or out-of-plane (along the *z* axis). DFT calculations show that both situations can cause the coexistence of S_1 and S_2 modes in 3 L, suggesting that in-plane and out-of-plane mixtures have similar features in Raman spectroscopy.

Compared with scanning transmission electron microscopy (STEM) techniques in stacking identification, the use of the interlayer shear modes in Raman spectroscopy is noticeably much faster. Moreover, sometimes it is more accurate to use Raman spectroscopy for identifying the phase. For example, the ABCA (3R) and ABAC stacking orders present similar stimulated STEM images, but their Raman features are quite different: The S_3 mode is the strongest in the 3R phase, while the S_2 mode dominates in the ABAC stacking [151].

We note that the above analysis is not only applicable to $MoSe_2$ [151, 180], but also suitable for graphene [187, 188], as demonstrated by experimental results. Subsequently, a correlation analysis between stacking and interlayer vibrational modes was performed on MoS_2 [181, 189]. For other 2D layered materials, such as ReS_2, recent studies suggest that the 2-fold

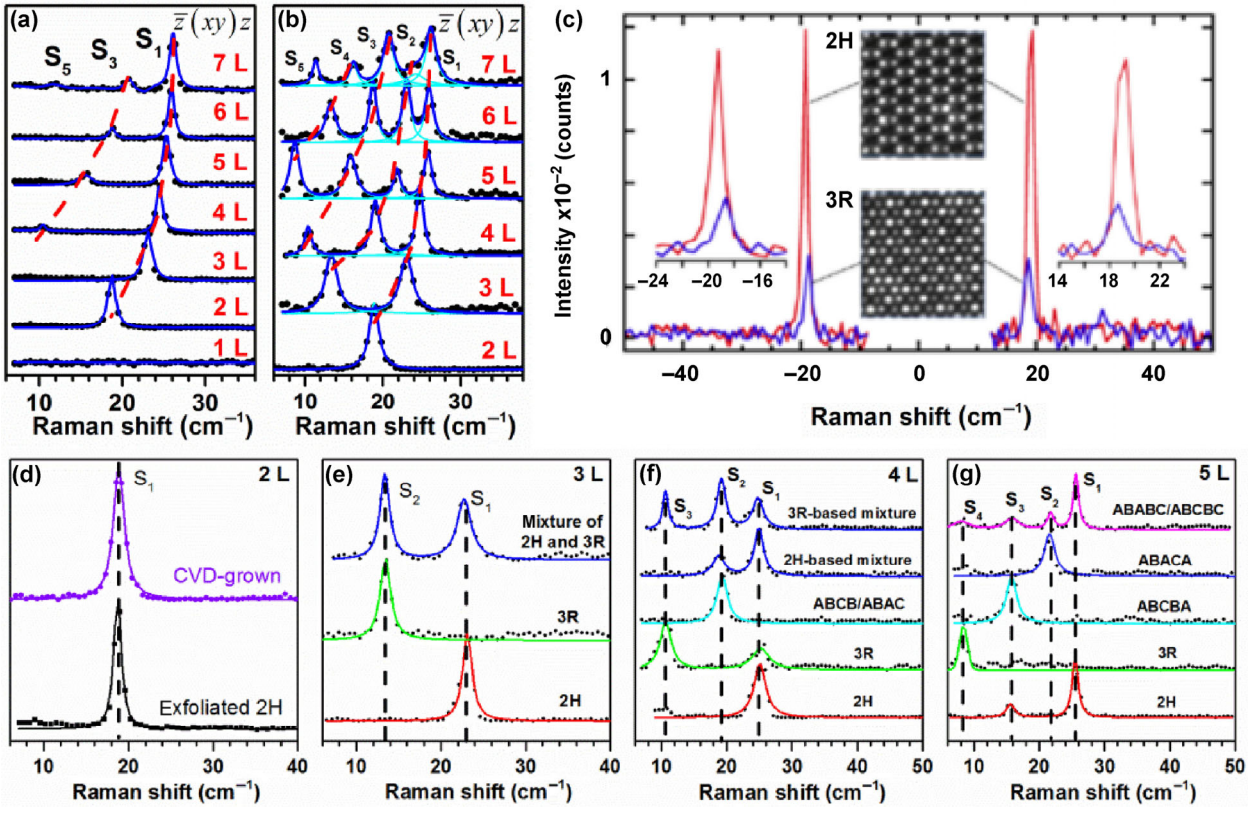

Figure 16 Raman spectra of few-layer $MoSe_2$ with different stacking orders. (a) and (b) Raman spectra of mono- and few-layer $MoSe_2$ from (a) mechanically exfoliated 2H-phase crystals and (b) CVD synthesis in the cross-polarized $\bar{z}(xy)z$ configuration. As different Raman features can be observed for flakes with the same thickness (owing to different stacking orders), in Fig. 16(b), we only show the spectra with the maximal number of observable interlayer shear modes in each case. (c) Raman spectra of 2 L $MoSe_2$ measured on a TEM grid for 2H and 3R stacking patterns, verified by atomic resolution STEM. (d) Raman spectra of CVD-grown and 2H-exfoliated $MoSe_2$ bilayers. (e)–(g) Raman spectra of CVD-grown 3 L (e), 4 L (f), and 5 L (g) $MoSe_2$ samples with different stacking. The dots in (a), (b) and (d)–(g) are experimental data and the lines are the fits to Lorentzian functions. (a), (b), and (d)–(g) are adapted from Ref. [151] with permission, © John Wiely & Sons, Inc 2015. (c) is adapted from Ref. [180] with permission, © American Chemical Society 2015.

degeneracy of the interlayer shear mode is broken, owing to the anisotropic distorted 1T structure [190, 191]. By comparison, the degeneracy is preserved in the isotropic-like stacked structure (also stable in ReS_2) [191].

Recent reports on twisted bilayer MoS_2 and $MoSe_2$ have demonstrated that the twist (stacking) angle can affect both the frequency and Raman intensity of the low-frequency interlayer vibrational modes [182, 183]. Both samples show that the variation is more sensitive when the twist angle is around 60° (and around 0° as well in MoS_2). When the twist angle is between 20° and 40° in MoS_2 (10°–50° in $MoSe_2$), the interlayer coupling is nearly constant as the stacking angle results in mismatched lattices over the entire sample. In contrast, the high-frequency intralayer vibrational modes are not as sensitive to the twist angle, similar to what has been observed in thickness-dependent Raman spectra. An earlier report, published in 2015, showed that the frequency of the interlayer breathing mode in a $MoS_2/MoSe_2$ bilayer heterostructure is angle-dependent [168], further confirming that the twist (stacking) angle affects the interlayer force constants in layered materials.

Finally, while the above discussion has focused on non-resonant Raman intensities, we should mention here that in twisted bilayer graphene, van Hove singularities in the band structure lead to resonant Raman transitions [75].

3.6 Polarization dependence

As we have discussed in Section 2.2, the detection of

a phonon mode in Raman spectroscopy depends on $\left|\boldsymbol{e}_{\mathrm{i}} \cdot \tilde{\boldsymbol{R}} \cdot \boldsymbol{e}_{\mathrm{s}}\right|^2$. The Raman tensor $\tilde{\boldsymbol{R}}$ is determined by the crystal symmetry, while $\boldsymbol{e}_{\mathrm{i}}$ and $\boldsymbol{e}_{\mathrm{s}}$ are related to the "polarization" that we will discuss in this section.

In both MX_2 (M = Mo, W; X = S, Se, Te) and Bi_2X_3 (X = Se, Te) systems, the z (c) axis is along the out-of-plane direction. The x, y, and z axes are chosen following the principal axes for all the crystal classes defined by Nye in 1957. More importantly, the Raman tensors were obtained based on these defined axes [66]. When we utilize the backscattering configuration for the Raman measurements on MX_2 (M = Mo, W; X = S, Se, Te) and Bi_2X_3 (X = Se, Te), parallel- and cross-polarized configurations are referred to $\bar{z}(xx)z$ and $\bar{z}(xy)z$, respectively, as we have mentioned in Section 2.2.

Figure 17 shows the polarization-dependent Raman spectra of 2H-MoS_2. The low-frequency interlayer breathing mode and the out-of-plane A_{1g} modes are both suppressed in the $\bar{z}(xy)z$ configuration. Compared with the in-plane modes, the out-of-plane modes do not have off-diagonal matrix elements in the Raman tensors, rendering $\left|\boldsymbol{e}_{\mathrm{i}} \cdot \tilde{\boldsymbol{R}} \cdot \boldsymbol{e}_{\mathrm{s}}\right|^2$ zero in the $\bar{z}(xy)z$ polarization configuration. Thus the breathing modes are suppressed in the cross-polarized configuration. In contrast, the in-plane modes are substantially strong in both polarization configurations.

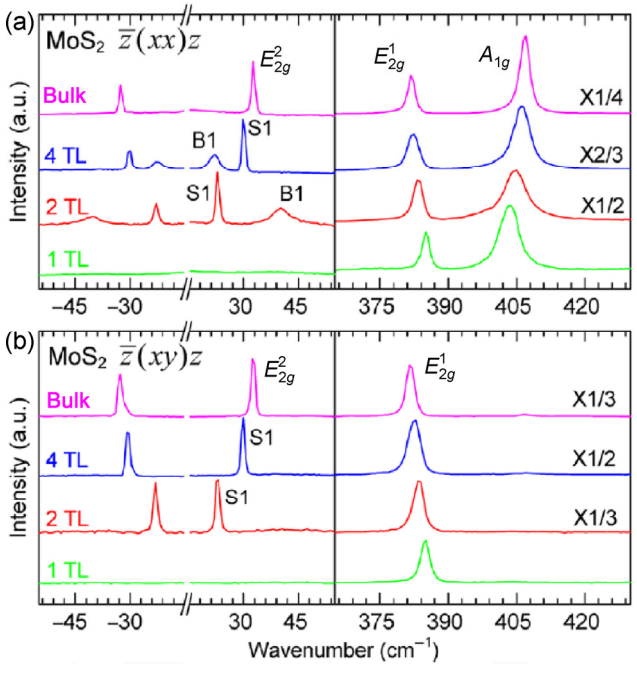

Figure 17 Polarization-dependent phonon modes in MoS_2. (a) and (b) Raman spectra of MoS_2 with different thicknesses, in the $\bar{z}(xx)z$ (a) and $\bar{z}(xy)z$ (b) polarization configurations. Reproduced with permission from Ref. [84], © American Chemical Society 2013.

By fixing the incident light and the scattered signal's polarization directions, such as in the parallel-polarized configuration, and by rotating the samples, we performed angle-dependent Raman measurements, where we changed the angle θ between the in-plane axis of the crystal and the polarization direction of the incident (and outgoing) light. In systems with strong in-plane anisotropy, such as in distorted 1T phase ReS_2 and $ReSe_2$ [190–194], or in black phosphorous [147, 195–197], the Raman spectra strongly depend on θ. In contrast, in samples that are less anisotropic in the basal plane, such as in 2H-MX_2 (M = Mo, W; X = S, Se, Te) and Bi_2X_3 (X = Se, Te), the Raman spectra shows a weak dependence on θ.

We focus our discussion here on black phosphorus. Note that the out-of-plane direction is defined to be the y axis for black phosphorus, different from that in MX_2 (M = Mo, W; X = S, Se, Te) and Bi_2X_3 (X = Se, Te). Although different ways have been previously proposed for assigning the axes in black phosphorus, according to the point group analysis, in the D_{2h} group (bulk: D^{18}_{2h}; odd number of layers: D^{7}_{2h}; even number of layers: D^{11}_{2h}), if there are three C_2 axes, the one with the largest number of unmoved atoms by the operation is the z (c) axis. The y (b) axis is defined as that axis of the remaining two C_2 axes which has the larger number of unmoved atoms by σ symmetry operations. Therefore, in black phosphorus, the y axis should be along the out-of-plane direction, with the x axis and z axis parallel to the zigzag and armchair edges, respectively. The Raman tensors of black phosphorus obtained with the set of axes using this convention [66], are

$$A_g: \begin{pmatrix} a & 0 & 0 \\ 0 & b & 0 \\ 0 & 0 & c \end{pmatrix} \quad B_{1g}: \begin{pmatrix} 0 & a & 0 \\ a & 0 & 0 \\ 0 & 0 & 0 \end{pmatrix}$$

$$B_{2g}: \begin{pmatrix} 0 & 0 & a \\ 0 & 0 & 0 \\ a & 0 & 0 \end{pmatrix} \quad B_{3g}: \begin{pmatrix} 0 & 0 & 0 \\ 0 & 0 & a \\ 0 & a & 0 \end{pmatrix}$$

So the A_g, B_{1g}, B_{2g}, and B_{3g} modes are Raman-active in the $\bar{y}(xx)y$, $\bar{z}(xy)z$, $\bar{y}(xz)y$ and $\bar{x}(yz)x$ polarization configurations, respectively.

After calculating $\left|\boldsymbol{e}_i \cdot \tilde{\boldsymbol{R}} \cdot \boldsymbol{e}_s\right|^2$, the Raman intensities of phonon modes in black phosphorus in the parallel configuration are

$$I_{B_{2g}} \propto \left|d \sin 2\theta\right|^2 \propto \left|\sin 2\theta\right|^2 \tag{9}$$

$$I_{A_g} \propto \left|a \cos^2\theta + c \sin^2\theta\right|^2 \propto \left|1 + \left(\frac{c}{a} - 1\right)\sin^2\theta\right|^2 \tag{10}$$

Similarly, we obtain that I_{A_g} and $I_{B_{2g}}$ are proportional to $\left|\sin 2\theta\right|^2$ and $\left|\cos 2\theta\right|^2$ in the cross-polarized configuration (with $\boldsymbol{e}_s$ being $(\sin\theta \;\; 0 \;\; -\cos\theta)$), respectively. We note that the components of the Raman tensor can be complex, owing to the influence of light absorption on the dielectric constants [195].

Experiments have also confirmed that the intensity of the low-frequency interlayer breathing mode A_g^3 also exhibits angular dependence, as shown in Fig. 19(b) and is consistent with the literature [135, 136]. Similar to the high-frequency A_g^2 mode [195, 197], a local maximum occurs at the angle perpendicular to that of the global maximum in the A_g^3 mode. Different from Fig. 18, the starting angle 0° is selected randomly in Fig. 19. Nevertheless, this does not affect the angle-dependent Raman intensity of the A_g^3 and A_g^2 modes: In the parallel-polarization configuration, the variation period of maximal (or 2nd maximal) intensity is 180°, and there is a 90° difference between the maximal intensity and the 2nd maximal intensity.

There has been a debate on the correlation of this result with the actual crystalline orientation. References [18, 135, 197] state that the maximal intensity of the A_g^2 (A_g^3) mode occurs when the polarization of incident light is along the armchair direction, while Ref. [195] comments that it is the zigzag direction that corresponds to the maximal intensity. Recently, it has been found that angle-dependent electron–photon and electron–phonon interactions in black phosphorus cause the angle-dependent Raman spectra to change with the thickness of the black phosphorus film and with the excitation laser energy [147].

The polarization dependence we discussed above involved linearly polarized light. It is interesting to

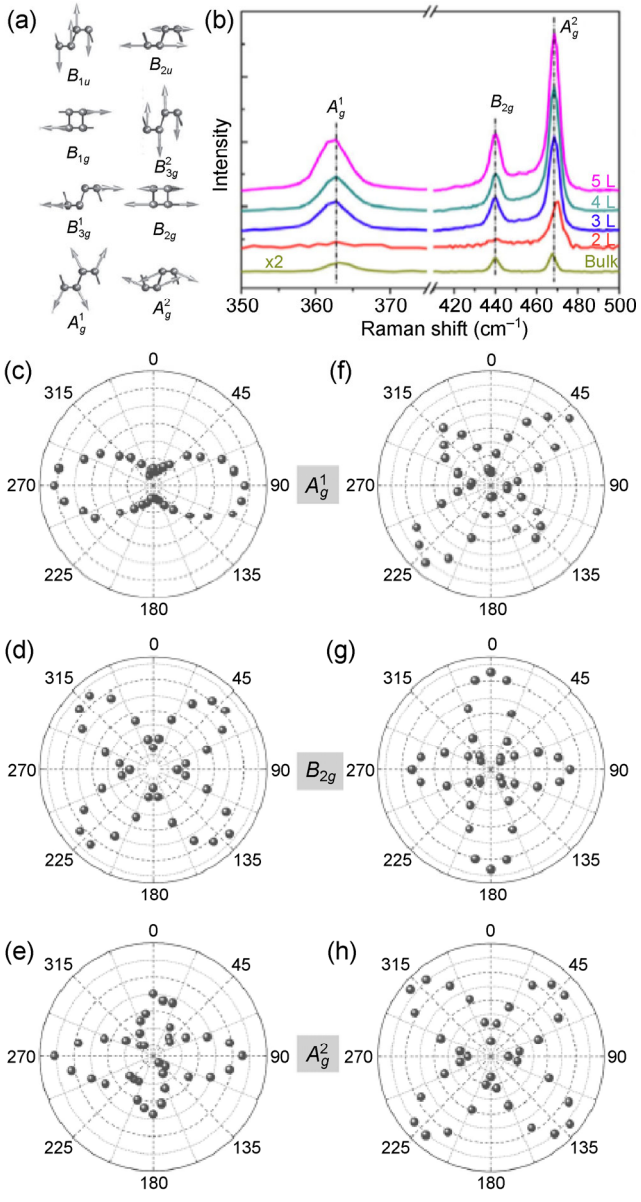

Figure 18 Vibrational Raman modes in black phosphorus. (a) Atomic displacement of the optical modes in black phosphorus (reproduced with permission from Ref. [196], © John Wiley & Sons, Inc 2015). (b) Raman spectra of 2–5 L and bulk black phosphorus (reproduced with permission from Ref. [130], © Tsinghua University Press and Springer-Verlag Berlin Heidelberg 2014). (c)–(h) Polar plots of the fitted peak intensities of A_g^1 (c) and (f), B_{2g} (d) and (g), and A_g^2 (e) and (h) modes versus the sample rotation, in the parallel (c)–(e) and cross-polarization (f)–(h) configurations. For the parallel-polarization configuration (c)–(e), when θ = 0°, the incident and outgoing beams of light are both parallel to the zigzag edge (x axis), and perpendicular to the armchair edge (z axis). For the cross-polarization configuration (f)–(h), when θ = 0°, the incident light is parallel to the zigzag edge (x axis), and the outgoing light is parallel to the armchair edge (z axis) (reproduced with permission from Ref. [197], © John Wiley & Sons, Inc 2015).

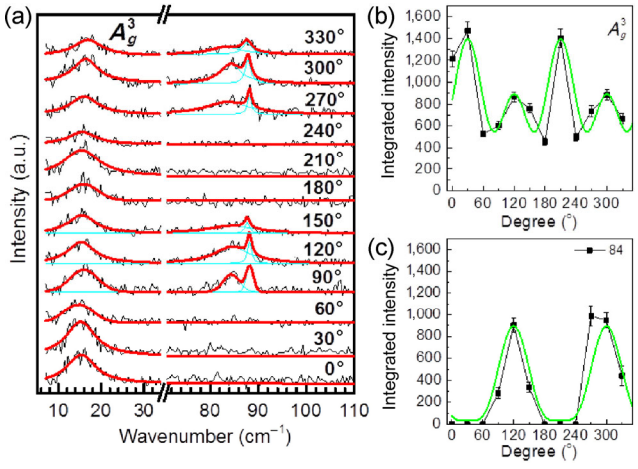

Figure 19 Anisotropic behavior of the A_g^3 mode. (a) Angle-dependent low-frequency Raman spectra of an 11 L black phosphorus thin flake in the parallel-polarization configuration. The black curves represent the experimental data, and the red lines are the Lorentzian fits. (b) and (c) The corresponding angular dependence of the interlayer mode A_g^3 (b) and an unknown mode near 84 cm^{-1} (c) for the 11 L black phosphorus thin flake. The black dots and lines are from the experimental data, while the green ones are the guiding lines. Note that the starting angle 0° is selected randomly. Polarization of incident and scattered light is fixed (parallel polarization). The angle was recorded according to by how many degrees had the sample rotated.

consider how the Raman spectra would change in the case of a circularly polarized laser beam, given that circularly polarized photoluminescence from atomically thin MoS_2 [22–24], WS_2 [198], and WSe_2 [4, 199] has been observed. Chen et al. have performed helicity-resolved Raman scattering measurements of 1–4 L 2H-MX_2 (M = Mo, W; X = S, Se) [149]. The results show that both intralayer and interlayer phonon modes depend on helicity. For the out-of-plane modes, the incident and scattered light have the same helicity, while for the in-plane modes, the incident and scattered light have opposite helicities. To understand this circular polarization dependence, we considered $\left|\boldsymbol{e}_i^{\dagger}\cdot\tilde{\boldsymbol{R}}\cdot\boldsymbol{e}_s\right|^2$, similar to the discussion above. If we take the out-of-plane A_{1g} mode in 2H-MoS_2 (Raman tensor shown in Section 3.3) as an example. For the circular polarization, the intensity is proportional to $\left|e_i^{\dagger}\cdot\tilde{R}\cdot e_s\right|^2$.

If both e_i and e_s are the left circular polarization. The $e_i = e_s = \frac{1}{\sqrt{2}}\begin{pmatrix}1\\ i\\ 0\end{pmatrix}$.

$$e_i^{\dagger}\cdot\tilde{R}\cdot e_s = \frac{1}{2}\begin{pmatrix}1 & -i & 0\end{pmatrix}\begin{pmatrix}a & 0 & 0\\ 0 & a & 0\\ 0 & 0 & b\end{pmatrix}\begin{pmatrix}1\\ i\\ 0\end{pmatrix} = a$$

If e_i and e_s are the left polarization and right circular polarization, respectively, then $e_i = \frac{1}{\sqrt{2}}\begin{pmatrix}1\\ i\\ 0\end{pmatrix}$ and $e_s = \frac{1}{\sqrt{2}}\begin{pmatrix}1\\ -i\\ 0\end{pmatrix}$.

$$e_i^{\dagger}\cdot\tilde{R}\cdot e_s = \frac{1}{2}\begin{pmatrix}1 & -i & 0\end{pmatrix}\begin{pmatrix}a & 0 & 0\\ 0 & a & 0\\ 0 & 0 & b\end{pmatrix}\begin{pmatrix}1\\ -i\\ 0\end{pmatrix} = 0$$

3.7 Resonance effects

In resonant Raman scattering, real electronic states, instead of virtual ones, are involved. Incoming resonance occurs when the energy of the incident photon beam (E_{laser}) matches the exciton energy ($E_{laser} = E_x$). Here, we define the exciton energy to be the energy level of the excitonic state relative to the valence band's maximum. Outgoing resonance occurs when $E_{laser} = E_x + E_{phonon}$ or $E_{laser} = E_x - E_{phonon}$. Mathematically, in the absence of damping, and in the presence of exciton–phonon coupling, the resonant Raman scattering probability will go to infinity. Experimentally, the enhancement factor is often several orders of magnitude [200].

The energy of the A (B) exciton in MoS_2 is ~1.88 eV (~2.06 eV). Resonant Raman scattering of MoS_2 can therefore be achieved by using both a 633 nm laser (1.96 eV) and a 594 nm laser (2.09 eV). The resonance window for WS_2 is even larger, from 1.96 to 2.41 eV. This is because the excitonic gaps for the A and B excitons in WS_2 are 1.95 eV and 2.36 eV at room temperature [95, 201].

Much work has been done to characterize resonant Raman scattering of MX_2 (M = Mo, W; X = S, Se) [94, 95, 201–203], including thickness dependence from bulk to monolayer, and temperature dependence from 300 to 4 K. Figure 20 shows the Raman spectra of MoS_2, comparing the non-resonance with resonance spectra.

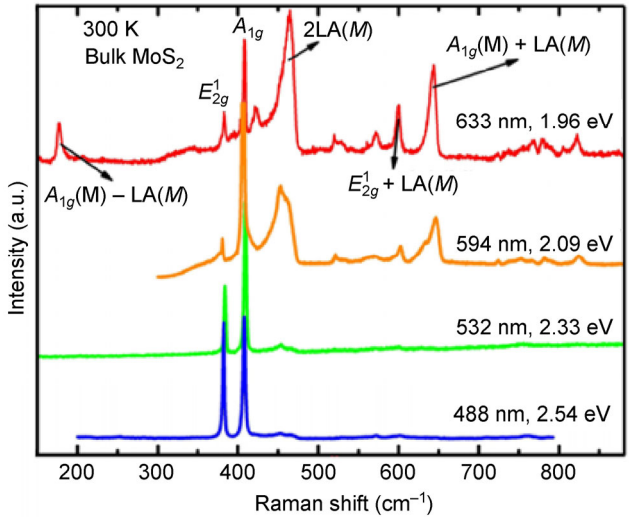

Figure 20 Raman spectra of bulk MoS_2 crystals, for different excitation wavelengths, at room temperature (reproduced with permission from Ref. [201], © AIP Publishing LLC 2014).

Similar to resonant Raman spectroscopy of other materials, the general features of resonant Raman spectra include: 1. Broad linewidth owing to the enhanced electron–phonon coupling; 2. the $k \approx 0$ Raman selection rule can be relaxed during high-order multi-phonon scattering processes when $\sum_i k_i \approx 0$. This explains why overtone or combination modes of the zone edge acoustic phonons are observed, such as 2LA(M) and $A_{1g}(M)+\mathrm{LA}(M)$ peaks in TMDs. Details on the assignment can be found in Refs. [25, 155]. In addition, a comprehensive study of resonant Raman spectroscopy on a few-layer MoS_2 with frequency in the range of 5–900 cm^{-1} is reported in a recent paper [204].

Next, we discuss the phenomena that are unique to TMD thin films, namely, the splitting of the monolayer out-of-plane A_1' mode in the few-layer WS_2 system [205]. In an N-layer WS_2 there are N zone center phonons evolving from the A_1' monolayer mode. As for bulk WS_2, the A_1' monolayer mode evolves into the in-phase and out-of-phase A_{1g}/B_{1u} pair, the so-called Davydov pair, which we have mentioned above. B_{1u} and A_{2u} are supposed to be the IR-active and Raman-inactive modes, respectively. However, in few-layer WS_2, all of the N components that evolve from the monolayer out-of-plane A_1' mode can be observed irrespective of their Raman activity, when the incident laser energy is close to the A exciton energy. These results are shown in Fig. 21. One possible explanation for the observation of all the N modes is related to the orientation of the excitons. Previous reports reveal that the excitons are entirely confined in plane, without significant expansion in the stacking direction of individual layers [206]. The wave function of the A exciton, although being spread out over a large area in two dimensions, has negligible density in the neighboring layers [207]. The non-zero coupling between the A exciton and the monolayer A_1' mode can, thus, lead to resonant Raman scattering for all N modes that evolve from A_1', because all of the N modes have the same form of the eigenmode displacement within each layer (differing only in the relative phases between layers).

Exciton–phonon coupling has also been observed in MoS_2. Carvalho et al. have used more than 30 excitation lines to measure the Raman excitation profile of the E_{2g}^1 and A_{1g} modes in MoS_2 systems with different thickness [208]. Results show that the Raman intensity of the A_{1g} mode is enhanced more than that of the E_{2g}^1 mode in the condition of resonance with A and B excitons. The stronger coupling effect in the case of the A_{1g} mode is related to the origin of the exciton. The A and B excitons originate from the K point in the Brillouin zone, and the conduction band minimum at the K point is primarily composed of d_{z^2} orbitals from Mo atoms, with out-of-plane orientation. Thus, the out-of-plane lattice vibration in the A_{1g} mode causes stronger coupling to the A/B excitons, compared with the E_{2g}^1 mode. Similar results were also obtained for $MoSe_2$ [209]. In contrast to the A and B excitons, the C exciton, originating from the Γ–□ line in the Brillouin zone, is less confined to one specific layer and is more extended over all of the N layers. Resonance with the C exciton can give rise to the interlayer resonant Raman modes, such as the E_g/E' mode in MoS_2 [210].

We remark that much work has been performed on resonant Raman scattering in atomically thin TMDs. Besides what we have mentioned, the resonant Ramnan effect on WSe_2 has been studied by del Corro et al. [211, 212], and a recent paper by Song et al. has discussed the Davydov splitting in the resonant Raman spectra of $MoTe_2$ [213]. Also, we would like to note that double resonance Raman spectroscopy of graphene is an active field of research [75, 214–216], while double resonance Raman scattering in monolayer WSe_2 was

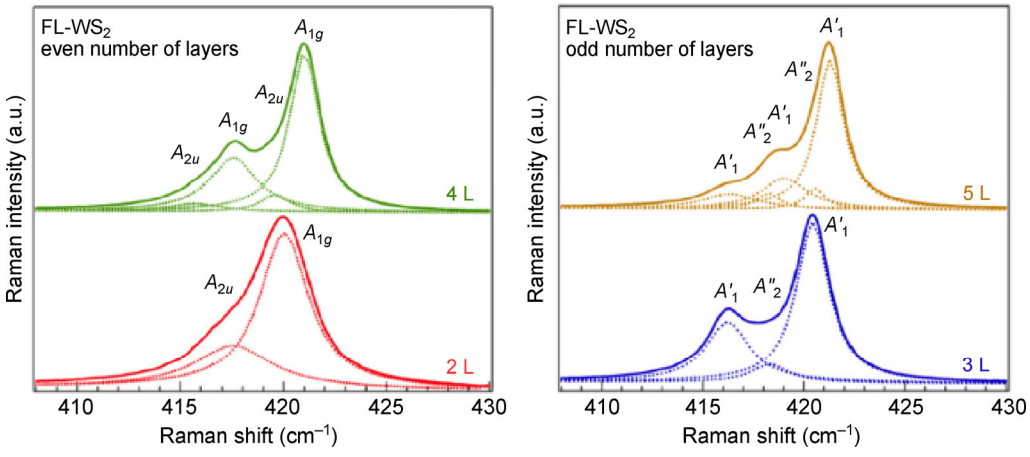

Figure 21 Raman spectra of few-layer WS_2 in the range of 408–430 cm^{-1}, with a 633-nm-wavelength laser as the excitation laser (reproduced with permission from Ref. [205], © American Physical Society 2015).

reported recently as well [217]. Moreover, triple resonance Raman scattering in MoS_2 has been revealed by using a 325-nm-wavelength laser [218].

4 Summary

We have provided a comprehensive review of lattice vibrational modes of mono- and few-layer thin flakes of group VI TMDs, 2D topologically insulating Bi_2X_3 (X = Se or Te), and black phosphorus. The general features were discussed in detail, including phonon confinement effects, anomalous frequency trends, surface effects, substrate effects, relation between stacking orders and interlayer shear modes, polarization dependence, as well as resonance effects. We believe that by delicate classification and by performing a variety of comparisons, we have provided a clear and comprehensive overview of recent studies of phonon properties in 2D thin layers beyond graphene.

Such fundamental studies, in addition to further investigations on the influence of temperature [219–222], pressure [223, 224], strain [225–228], and doping [138, 229–231] on the phonon modes in 2D materials, will be important for establishing a basic understanding of phonons and their coupling to other elementary excitations. In addition, the fundamental studies of phonon properties in 2D thin layers can be further extended by exploring multilayer heterostructures [232]. Future advances in the exquisite control of homogeneous or heterogeneous layered crystals or their heterostructures will enable unprecedented opportunities to probe the lattice dynamics and the electron–phonon or exciton–phonon interactions in these materials, paving the way towards applications in electronic, photonic or valleytronic devices.

Acknowledgements

Q. H. X. gratefully thanks Singapore National Research Foundation via a Fellowship grant (No. NRF-RF2009-06) and an Investigatorship grant (No. NRF-NRFI2015-03), Ministry of Education via a tier2 grant (No. MOE2012-T2-2-086) and a tier1 grant (No. 2013-T1-002-232). S. Y. Q. and X. Luo gratefully acknowledge the Singapore National Research Foundation (NRF) for funding under the NRF Fellowship (No. NRF-NRFF2013-07). Z. J. gratefully thanks National Natural Science Foundation of China (Nos. 11574305 and 51527901) and financial support from the National 1000 Talent Plan of China via a Young Project. The computations were performed on the cluster of NUS Graphene Research Centre. S. Y. Q. and X. Luo acknowledge the National Research Foundation, Prime Minister's Office, Singapore, under its Medium Sized Centre Programme.

References

[1] Geim, A. K.; Novoselov, K. S. The rise of graphene. *Nat. Mater.* **2007**, *6*, 183–191.

[2] Wang, Q. H.; Kalantar-Zadeh, K.; Kis, A.; Coleman, J. N.; Strano, M. S. Electronics and optoelectronics of two-dimensional transition metal dichalcogenides. *Nat. Nanotechnol.* **2012**, *7*, 699–712.

[3] Chhowalla, M.; Shin, H. S.; Eda, G.; Li, L. J.; Loh, K. P.; Zhang, H. Z. The chemistry of two-dimensional layered transition metal dichalcogenide nanosheets. *Nat. Chem.* **2013**, *5*, 263–275.

[4] Xu, X. D.; Yao, W.; Xiao, D.; Heinz, T. F. Spin and pseudospins in layered transition metal dichalcogenides. *Nat. Phys.* **2014**, *10*, 343–350.

[5] Liu, H.; Du, Y. C.; Deng, Y. X.; Ye, P. D. Semiconducting black phosphorus: Synthesis, transport properties and electronic applications. *Chem. Soc. Rev.* **2015**, *44*, 2732–2743.

[6] Ling, X.; Wang, H.; Huang, S. X.; Xia, F. N.; Dresselhaus, M. S. The renaissance of black phosphorus. *Proc. Natl. Acad. Sci. USA* **2015**, *112*, 4523–4530.

[7] Geim, A. K.; Grigorieva, I. V. Van der Waals heterostructures. *Nature* **2013**, *499*, 419–425.

[8] Zhang, Y.; He, K.; Chang, C.-Z.; Song, C.-L.; Wang, L.-L.; Chen, X.; Jia, J.-F.; Fang, Z.; Dai, X.; Shan, W.-Y. et al. Crossover of the three-dimensional topological insulator Bi_2Se_3 to the two-dimensional limit. *Nat. Phys.* **2010**, *6*, 584–588.

[9] Huang, X.; Zhang, H. Molecular crystals on two-dimensional van der Waals substrates. *Sci. China Mater.* **2015**, *58*, 5–8.

[10] Novoselov, K. S.; Jiang, Z.; Zhang, Y.; Morozov, S. V.; Stormer, H. L.; Zeitler, U.; Maan, J. C.; Boebinger, G. S.; Kim, P.; Geim, A. K. Room-temperature quantum hall effect in graphene. *Science* **2007**, *315*, 1379–1379.

[11] Hasan, M. Z.; Kane, C. L. Colloquium: Topological insulators. *Rev. Mod. Phys.* **2010**, *82*, 3045–3067.

[12] Qi, X.-L.; Zhang, S.-C. Topological insulators and superconductors. *Rev. Mod. Phys.* **2011**, *83*, 1057–1110.

[13] Splendiani, A.; Sun, L.; Zhang, Y. B.; Li, T. S.; Kim, J.; Chim, C.-Y.; Galli, G.; Wang, F. Emerging photoluminescence in monolayer MoS_2. *Nano Lett.* **2010**, *10*, 1271–1275.

[14] Mak, K. F.; Lee, C.; Hone, J.; Shan, J.; Heinz, T. F. Atomically thin MoS_2: A new direct-gap semiconductor. *Phys. Rev. Lett.* **2010**, *105*, 136805.

[15] Gutiérrez, H. R.; Perea-López, N.; Elías, A. L.; Berkdemir, A.; Wang, B.; Lv, R. T.; López-Urías, F.; Crespi, V. H.; Terrones, H.; Terrones, M. Extraordinary room-temperature photoluminescence in triangular WS_2 monolayers. *Nano Lett.* **2013**, *13*, 3447–3454.

[16] Li, L. K.; Yu, Y. J.; Ye, G. J.; Ge, Q. Q.; Ou, X. D.; Wu, H.; Feng, D. L.; Chen, X. H.; Zhang, Y. B. Black phosphorus field-effect transistors. *Nat. Nanotechnol.* **2014**, *9*, 372–377.

[17] Liu, H.; Neal, A. T.; Zhu, Z.; Luo, Z.; Xu, X. F.; Tománek, D.; Ye, P. D. Phosphorene: An unexplored 2D semiconductor with a high hole mobility. *ACS Nano* **2014**, *8*, 4033–4041.

[18] Wang, X. M.; Jones, A. M.; Seyler, K. L.; Tran, V.; Jia, Y. C.; Zhao, H.; Wang, H.; Yang, L.; Xu, X. D.; Xia, F. N. Highly anisotropic and robust excitons in monolayer black phosphorus. *Nat. Nanotechnol.* **2015**, *10*, 517–521.

[19] Xia, F. N.; Wang, H.; Jia, Y. C. Rediscovering black phosphorus as an anisotropic layered material for optoelectronics and electronics. *Nat. Commun.* **2014**, *5*, 4458.

[20] Ando, T.; Fowler, A. B.; Stern, F. Electronic properties of two-dimensional systems. *Rev. Mod. Phys.* **1982**, *54*, 437–672.

[21] Kim, S.; Konar, A.; Hwang, W. S.; Lee, J. H.; Lee, J.; Yang, J.; Jung, C.; Kim, H.; Yoo, J. B.; Choi, J. Y. et al. High-mobility and low-power thin-film transistors based on multilayer MoS_2 crystals. *Nat. Commun.* **2012**, *3*, 1011.

[22] Mak, K. F.; He, K. L.; Shan, J.; Heinz, T. F. Control of valley polarization in monolayer MoS_2 by optical helicity. *Nat. Nanotechnol.* **2012**, *7*, 494–498.

[23] Zeng, H. L.; Dai, J. F.; Yao, W.; Xiao, D.; Cui, X. D. Valley polarization in MoS_2 monolayers by optical pumping. *Nat. Nanotechnol.* **2012**, *7*, 490–493.

[24] Cao, T.; Wang, G.; Han, W. P.; Ye, H. Q.; Zhu, C. R.; Shi, J. R.; Niu, Q.; Tan, P. H.; Wang, E. G.; Liu, B. L. et al. Valley-selective circular dichroism of monolayer molybdenum disulphide. *Nat. Commun.* **2012**, *3*, 887.

[25] Zhang, X.; Qiao, X.-F.; Shi, W.; Wu, J.-B.; Jiang, D.-S.; Tan, P.-H. Phonon and Raman scattering of two-dimensional transition metal dichalcogenides from monolayer, multilayer to bulk material. *Chem. Soc. Rev.* **2015**, *44*, 2757–2785.

[26] Molina-Sánchez, A.; Hummer, K.; Wirtz, L. Vibrational and optical properties of MoS_2: From monolayer to bulk. *Surf. Sci. Rep.* **2015**, *70*, 554–586.

[27] Ji, J. T.; Dong, S.; Zhang, A. M.; Zhang, Q. M. Low-frequency interlayer vibration modes in two-dimensional layered materials. *Phys. E* **2016**, *80*, 130–141.

[28] Zhang, X.; Tan, Q.-H.; Wu, J.-B.; Shi, W.; Tan, P.-H. Review on the Raman spectroscopy of different types of layered materials. *Nanoscale* **2016**, *8*, 6435–6450.

[29] Luo, X.; Lu, X.; Koon, G. K. W.; Neto, A. H. C.; Özyilmaz, B.; Xiong, Q. H.; Quek, S. Y. Large frequency change with thickness in interlayer breathing mode-significant interlayer interactions in few layer black phosphorus. *Nano Lett.* **2015**, *15*, 3931–3938.

[30] Zhang, H. J.; Liu, C.-X.; Qi, X.-L.; Dai, X.; Fang, Z.; Zhang, S.-C. Topological insulators in Bi_2Se_3, Bi_2Te_3 and Sb_2Te_3 with a single Dirac cone on the surface. *Nat. Phys.* **2009**, *5*, 438–442.

[31] Chen, Y. L.; Analytis, J. G.; Chu, J. H.; Liu, Z. K.; Mo, S. K.; Qi, X. L.; Zhang, H. J.; Lu, D. H.; Dai, X.; Fang, Z. et al. Experimental realization of a three-dimensional topological

insulator, Bi_2Te_3. *Science* **2009**, *325*, 178–181.

[32] Keum, D. H.; Cho, S.; Kim, J. H.; Choe, D.-H.; Sung, H.-J.; Kan, M.; Kang, H.; Hwang, J.-Y.; Kim, S. W.; Yang, H. et al. Bandgap opening in few-layered monoclinic $MoTe_2$. *Nat. Phys.* **2015**, *11*, 482–486.

[33] Qian, X. F.; Liu, J. W.; Fu, L.; Li, J. Quantum spin Hall effect in two-dimensional transition metal dichalcogenides. *Science* **2014**, *346*, 1344–1347.

[34] Eda, G.; Yamaguchi, H.; Voiry, F.; Fujita, T.; Chen, M. W.; Chowalla, M. Photoluminescence from chemically exfoliated MoS_2. *Nano Lett.* **2011**, *11*, 5111–5116.

[35] Gupta, U.; Naidu, B. S.; Maitra, U.; Singh, A.; Shirodkar, S. N.; Waghmare, U. V.; Rao, C. N. R. Characterization of few-layer 1T-$MoSe_2$ and its superior performance in the visible-light induced hydrogen evolution reaction. *APL Mater.* **2014**, *2*, 092802.

[36] Shirodkar, S. N.; Waghmare, U. V. Emergence of ferroelectricity at a metal-semiconductor transition in a 1T monolayer of MoS_2. *Phys. Rev. Lett.* **2014**, *112*, 157601.

[37] Amara, K. K.; Chen, Y. F.; Lin, Y.-C.; Kumar, R.; Okunishi, E.; Suenaga, K.; Quek, S. Y.; Eda, G. Dynamic structural evolution of metal–metal bonding network in monolayer WS_2. *Chem. Mater.* **2016**, *28*, 2308–2314.

[38] Wilson, J. A.; Yoffe, A. D. The transition metal dichalcogenides discussion and interpretation of the observed optical, electrical and structural properties. *Adv. Phys.* **1969**, *18*, 193–335.

[39] Suzuki, R.; Sakano, M.; Zhang, Y. J.; Akashi, R.; Morikawa, D.; Harasawa, A.; Yaji, K.; Kuroda, K.; Miyamoto, K.; Okuda, T. et al. Valley-dependent spin polarization in bulk MoS_2 with broken inversion symmetry. *Nat. Nanotechnol.* **2014**, *9*, 611–617.

[40] Raman, C. V.; Krishnan, K. S. A new type of secondary radiation. *Nature* **1928**, *121*, 501–502.

[41] Raman, C. V. A change of wave-length in light scattering. *Nature* **1928**, *121*, 619.

[42] Cardona, M. *Light Scattering in Solids I*; Springer-Verlag: Berlin, 1983.

[43] Ferrari, A. C.; Robertson, J. Raman spectroscopy of amorphous, nanostructured, diamond-like carbon, and nanodiamond. *Phil. Trans. R. Soc. A* **2004**, *362*, 2477–2512.

[44] Ferrari, A. C. Raman spectroscopy of graphene and graphite: Disorder, electron–phonon coupling, doping and nonadiabatic effects. *Solid State Commun.* **2007**, *143*, 47–57.

[45] Ferrari, A. C.; Basko, D. M. Raman spectroscopy as a versatile tool for studying the properties of graphene. *Nat. Nanotechnol.* **2013**, *8*, 235–246.

[46] Malard, L. M.; Pimenta, M. A.; Dresselhaus, G.; Dresselhaus, M. S. Raman spectroscopy in graphene. *Phys. Rep.* **2009**, *473*, 51–87.

[47] Ni, Z. H.; Wang, Y. Y.; Yu, T.; Shen, Z. X. Raman spectroscopy and imaging of graphene. *Nano Res.* **2008**, *1*, 273–291.

[48] Dresselhaus, M. S.; Dresselhaus, G.; Saito, R.; Jorio, A. Raman spectroscopy of carbon nanotubes. *Phys. Rep.* **2005**, *409*, 47–99.

[49] Dresselhaus, M. S.; Eklund, P. C. Phonons in carbon nanotubes. *Adv. Phys.* **2000**, *49*, 705–814.

[50] Eklund, P. C.; Holden, J. M.; Jishi, R. A. Vibrational-modes of carbon nanotubes; Spectroscopy and theory. *Carbon* **1995**, *33*, 959–972.

[51] Chen, G.; Wu, J.; Lu, Q. J.; Gutierrez, H. R.; Xiong, Q. H.; Pellen, M. E.; Petko, J. S.; Werner, D. H.; Eklund, P. C. Optical antenna effect in semiconducting nanowires. *Nano Lett.* **2008**, *8*, 1341–1346.

[52] Jorio, A.; Souza Filho, A. G.; Brar, V. W.; Swan, A. K.; Ünlü, M. S.; Goldberg, B. B.; Righi, A.; Hafner, J. H.; Lieber, C. M.; Saito, R. et al. Polarized resonant Raman study of isolated single-wall carbon nanotubes: Symmetry selection rules, dipolar and multipolar antenna effects. *Phys. Rev. B* **2002**, *65*, 121402.

[53] Wang, R. P.; Xu, G.; Jin, P. Size dependence of electron–phonon coupling in ZnO nanowires. *Phys. Rev. B* **2004**, *69*, 113303.

[54] Zhang, Q.; Zhang, J.; Utama, M. I. B.; Peng, B.; de la Mata, M.; Arbiol, J.; Xiong, Q. H. Exciton–phonon coupling in individual ZnTe nanorods studied by resonant Raman spectroscopy. *Phys. Rev. B* **2012**, *85*, 085418.

[55] Chen, Y. Q.; Peng, B.; Wang, B. Raman spectra and temperature-dependent Raman scattering of silicon nanowires. *J. Phys. Chem. C* **2007**, *111*, 5855–5858.

[56] Zhang, Q.; Liu, X. F.; Utama, M. I. B.; Zhang, J.; de la Mata, M.; Arbiol, J.; Lu, Y. H.; Sum, T. C.; Xiong, Q. H. Highly enhanced exciton recombination rate by strong electron–phonon coupling in single ZnTe nanobelt. *Nano Lett.* **2012**, *12*, 6420–6427.

[57] Adu, K. W.; Gutiérrez, H. R.; Kim, U. J.; Eklund, P. C. Inhomogeneous laser heating and phonon confinement in silicon nanowires: A micro-Raman scattering study. *Phys. Rev. B* **2006**, *73*, 155333.

[58] Adu, K. W.; Xiong, Q.; Gutierrez, H. R.; Chen, G.; Eklund, P. C. Raman scattering as a probe of phonon confinement and surface optical modes in semiconducting nanowires. *Appl. Phys. A* **2006**, *85*, 287–297.

[59] Wang, R. P.; Zhou, G. W.; Liu, Y. L.; Pan, S. H.; Zhang, H. Z.; Yu, D. P.; Zhang, Z. Raman spectral study of silicon nanowires: High-order scattering and phonon confinement effects. *Phys. Rev. B* **2000**, *61*, 16827–16832.

[60] Piscanec, S.; Cantoro, M.; Ferrari, A. C.; Zapien, J. A.; Lifshitz, Y.; Lee, S. T.; Hofmann, S.; Robertson, J. Raman spectroscopy of silicon nanowires. *Phys. Rev. B* **2003**, *68*, 241312.

[61] Gupta, R.; Xiong, Q.; Adu, C. K.; Kim, U. J.; Eklund, P. C. Laser-induced Fano resonance scattering in silicon nanowires. *Nano Lett.* **2003**, *3*, 627–631.

[62] Xiong, Q. H.; Wang, J. G.; Reese, O.; Lew Yan Voon, L. C.; Eklund, P. C. Raman scattering from surface phonons in rectangular cross-sectional w-ZnS nanowires. *Nano Lett.* **2004**, *4*, 1991–1996.

[63] Gupta, R.; Xiong, Q. H.; Mahan, G. D.; Eklund, P. C. Surface optical phonons in gallium phosphide nanowires. *Nano Lett.* **2003**, *3*, 1745–1750.

[64] Ferraro, J. R.; Nakamoto, K.; Brown, C. W. *Introductory Raman Spectroscopy*, 2nd ed.; Elsevier: Amsterdam, 2003.

[65] Smith, E.; Dent, G. *Modern Raman Spectroscopy—A Practical Approach*; Wiley: Chichester, 2005.

[66] Loudon, R. The Raman effect in crystals. *Adv. Phys.* **2001**, *50*, 813–864.

[67] Wieting, T. J. Long-wavelength lattice vibrations of MoS_2 and GaSe. *Solid State Commun.* **1973**, *12*, 931–935.

[68] Nemanich, R. J.; Lucovsky, G.; Solin, S. A. Long Wavelength Lattice Vibrations of Graphite. In *Proceedings of the International Conference on Lattice Dynamics*, Paris, France, 1977, pp 619–621.

[69] Yu, P.; Cardona, M. *Fundamentals of Semiconductors: Physics and Materials Properties*, 4th ed.; Springer-Verlag: Berlin, 2010.

[70] Baroni, S.; de Gironcoli, S.; Dal Corso, A.; Giannozzi, P. Phonons and related crystal properties from density-functional perturbation theory. *Rev. Mod. Phys.* **2001**, *73*, 515–562.

[71] Brüesch, P. *Phonons: Theory and Experiments II: Experiments and Interpretation of Experimental Results*; Springer-Verlag: Berlin, 1986.

[72] Cardona, M.; Güntherodt, G. *Light Scattering in Solids II*; Springer-Verlag: Berlin, 1982.

[73] Luo, X.; Zhao, Y. Y.; Zhang, J.; Xiong, Q. H.; Quek, S. Y. Anomalous frequency trends in MoS_2 thin films attributed to surface effects. *Phys. Rev. B* **2013**, *88*, 075320.

[74] Umari, P.; Pasquarello, A.; Dal Corso, A. Raman scattering intensities in α-quartz: A first-principles investigation. *Phys. Rev. B* **2001**, *63*, 094305.

[75] Wu, J.-B.; Zhang, X.; Ijäs, M.; Han, W.-P.; Qiao, X.-F.; Li, X.-L.; Jiang, D.-S.; Ferrari, A. C.; Tan, P.-H. Resonant Raman spectroscopy of twisted multilayer graphene. *Nat. Commun.* **2014**, *5*, 5309.

[76] Coh, S.; Tan, L. Z.; Louie, S. G.; Cohen, M. L. Theory of the Raman spectrum of rotated double-layer graphene. *Phys. Rev. B* **2013**, *88*, 165431.

[77] Allard, A.; Wirtz, L. Graphene on metallic substrates: Suppression of the kohn anomalies in the phonon dispersion. *Nano Lett.* **2010**, *10*, 4335–4340.

[78] Kern, G.; Kresse, G.; Hafner, J. *Ab initio* calculation of the lattice dynamics and phase diagram of boron nitride. *Phys. Rev. B* **1999**, *59*, 8551–8559.

[79] Serrano, J.; Bosak, A.; Arenal, R.; Krisch, M.; Watanabe, K.; Taniguchi, T.; Kanda, H.; Rubio, A.; Wirtz, L. Vibrational properties of hexagonal boron nitride: Inelastic X-ray scattering and *ab initio* calculations. *Phys. Rev. Lett.* **2007**, *98*, 095503.

[80] Wirtz, L.; Rubio, A. The phonon dispersion of graphite revisited. *Solid State Commun.* **2004**, *131*, 141–152.

[81] Dion, M.; Rydberg, H.; Schröder, E.; Langreth, D. C.; Lundqvist, B. I. Van der Waals density functional for general geometries. *Phys. Rev. Lett.* **2004**, *92*, 246401.

[82] Cooper, V. R. Van der Waals density functional: An appropriate exchange functional. *Phys. Rev. B* **2010**, *81*, 161104(R).

[83] Grimme, S.; Antony, J.; Ehrlich, S.; Krieg, H. A consistent and accurate *ab initio* parametrization of density functional dispersion correction (DFT-D) for the 94 elements H-Pu. *J. Chem. Phys.* **2010**, *132*, 154104.

[84] Zhao, Y. Y.; Luo, X.; Li, H.; Zhang, J.; Araujo, P. T.; Gan, C. K.; Wu, J.; Zhang, H.; Quek, S. Y.; Dresselhaus, M. S. et al. Interlayer breathing and shear modes in few-trilayer MoS_2 and WSe_2. *Nano Lett.* **2013**, *13*, 1007–1015.

[85] Luo, X.; Sullivan, M. B.; Quek, S. Y. First-principles investigations of the atomic, electronic, and thermoelectric properties of equilibrium and strained Bi_2Se_3 and Bi_2Te_3 including van der Waals interactions. *Phys. Rev. B* **2012**, *86*, 184111.

[86] Verble, J. L.; Wieting, T. J. Lattice mode degeneracy in MoS_2 and other layer compounds. *Phys. Rev. Lett.* **1970**, *25*, 362–365.

[87] Wieting, T. J.; Verble, J. L. Infrared and Raman studies of long-wavelength optical phonons in hexagonal MoS_2. *Phys. Rev. B* **1971**, *3*, 4286–4292.

[88] Ghosh, P. N.; Maiti, C. R. Interlayer force and Davydov splitting in 2H-MoS_2. *Phys. Rev. B* **1983**, *28*, 2237–2239.

[89] Böker, T.; Severin, R.; Müller, A.; Janowitz, C.; Manzke, R.; Voβ, D.; Krüger, P.; Mazur, A.; Pollmann, J. Band structure of MoS_2, $MoSe_2$, and α-$MoTe_2$: Angle-resolved photoelectron spectroscopy and *ab initio* calculations. *Phys. Rev. B* **2001**, *64*, 235305.

[90] Sugai, S.; Ueda, T. High-pressure Raman-spectroscopy in the layered materials 2H-MoS_2, 2H-$MoSe_2$ and 2H-$MoTe_2$. *Phys. Rev. B* **1982**, *26*, 6554–6558.

[91] Sekine, T.; Nakashizu, T.; Toyoda, K.; Uchinokura, K.; Matsuura, E. Raman scattering in layered compound 2H-WS_2. *Solid State Commun.* **1980**, *35*, 371–373.

[92] Sourisseau, C.; Cruege, F.; Fouassier, M.; Alba, M. Second-order Raman effects, inelastic neutron-scattering and lattice-dynamics in 2H-WS_2. *Chem. Phys.* **1991**, *150*, 281–293.

[93] Chen, J. M.; Wang, C. S. Second-order Raman-spectrum of MoS_2. *Solid State Commun.* **1974**, *14*, 857–860.

[94] Frey, G. L.; Tenne, R.; Matthews, M. J.; Dresselhaus, M. S.; Dresselhaus, G. Raman and resonance Raman investigation of MoS_2 nanoparticles. *Phys. Rev. B* **1999**, *60*, 2883–2892.

[95] Frey, G. L.; Tenne, R.; Matthews, M. J.; Dresselhaus, M. S.; Dresselhaus, G. Optical properties of MS_2 (M = Mo, W) inorganic fullerenelike and nanotube material optical absorption and resonance Raman measurements. *J. Mater. Res.* **1998**, *13*, 2412–2417.

[96] Viršek, M.; Jesih, A.; Milošević, I.; Damnjanović, M.; Remškar, M. Raman scattering of the MoS_2 and WS_2 single nanotubes. *Surf. Sci.* **2007**, *601*, 2868–2872.

[97] Sandoval, S. J.; Yang, D.; Frindt, R. F.; Irwin, J. C. Raman-study and lattice-dynamics of single molecular layers of MoS_2. *Phys. Rev. B* **1991**, *44*, 3955–3962.

[98] Akahama, Y.; Kobayashi, M.; Kawamura, H. Raman study of black phosphorus up to 13 GPa. *Solid State Commun.* **1997**, *104*, 311–315.

[99] Vanderborgh, C. A.; Schiferl, D. Raman studies of black phosphorus from 0.25 to 7.7 Gpa at 15 k. *Phys. Rev. B* **1989**, *40*, 9595–9599.

[100] Sugai, S.; Ueda, T.; Murase, K. Pressure dependence of the lattice vibration in the orthorhombic and rhombohedral structures of black phosphorus. *J. Phys. Soc. Jpn.* **1981**, *50*, 3356–3361.

[101] Kaneta, C.; Katayama-Yoshida, H.; Morita, A. Lattice dynamics of black phosphorus. *Solid State Commun.* **1982**, *44*, 613–617.

[102] Sugai, S.; Shirotani, I. Raman and infrared reflection spectroscopy in black phosphorus. *Solid State Commun.* **1985**, *53*, 753–755.

[103] Wagner, V.; Dolling, G.; Powell, B. M.; Landwehr, G. Lattice vibrations of Bi_2Te_3. *Phys. Status Solidi B* **1978**, *85*, 311–317.

[104] Kullmann, W.; Geurts, J.; Richter, W.; Lehner, N.; Rauh, H.; Steigenberger, U.; Eichhorn, G.; Geick, R. Effect of hydrostatic and uniaxial pressure on structural properties and Raman active lattice vibrations in Bi_2Te_3. *Phys. Status Solidi B* **1984**, *125*, 131–138.

[105] Rauh, H.; Geick, R.; Kohler, H.; Nucker, N.; Lehner, N. Generalized phonon density of states of the layer compounds Bi_2Se_3, Bi_2Te_3, Sb_2Te_3 and $Bi_2(Te_{0.5}Se_{0.5})_3$, $(Bi_{0.5}Sb_{0.5})_2Te_3$. *J. Phys. C* **1981**, *14*, 2705–2712.

[106] Richter, W.; Becker, C. R. A Raman and far-infrared investigation of phonons in the rhombohedral V_2-VI_3 compounds Bi_2Te_3, Bi_2Se_3, Sb_2Te_3 and $Bi_2(Te_{1-x}Se_x)_3$ ($0 < x < 1$), $(Bi_{1-y}Sby)_2Te_3$ ($0 < y < 1$). *Phys. Status Solidi B* **1977**, *84*, 619–628.

[107] Michel, K. H.; Verberck, B. Theory of rigid-plane phonon modes in layered crystals. *Phys. Rev. B* **2012**, *85*, 094303.

[108] Luo, X.; Zhao, Y. Y.; Zhang, J.; Toh, M.; Kloc, C.; Xiong, Q. H.; Quek, S. Y. Effects of lower symmetry and dimensionality on Raman spectra in two-dimensional WSe_2. *Phys. Rev. B* **2013**, *88*, 195313.

[109] Verble, J. L.; Wietling, T. J.; Reed, P. R. Rigid-layer lattice vibrations and van der waals bonding in hexagonal MoS_2. *Solid State Commun.* **1972**, *11*, 941–944.

[110] Sekine, T.; Izumi, M.; Nakashizu, T.; Uchinokura, K.; Matsuura, E. Raman-scattering and Infrared reflectance in 2H-$MoSe_2$. *J. Phys. Soc. Jpn.* **1980**, *49*, 1069–1077.

[111] Mead, D. G.; Irwin, J. C. Long wavelength optic phonons in WSe_2. *Can. J. Phys.* **1977**, *55*, 379–382.

[112] Saha, S. K.; Waghmare, U. V.; Krishnamurthy, H. R.; Sood, A. K. Phonons in few-layer graphene and interplanar interaction: A first-principles study. *Phys. Rev. B* **2008**, *78*, 165421.

[113] Tan, P. H.; Han, W. P.; Zhao, W. J.; Wu, Z. H.; Chang, K.; Wang, H.; Wang, Y. F.; Bonini, N.; Marzari, N.; Pugno, N. et al. The shear mode of multilayer graphene. *Nat. Mater.* **2012**, *11*, 294–300.

[114] Zhang, X.; Han, W. P.; Wu, J. B.; Milana, S.; Lu, Y.; Li, Q. Q.; Ferrari, A. C.; Tan, P. H. Raman spectroscopy of shear and layer breathing modes in multilayer MoS_2. *Phys. Rev. B* **2013**, *87*, 115413.

[115] Zeng, H. L.; Zhu, B. R.; Liu, K.; Fan, J. H.; Cui, X. D.; Zhang, Q. M. Low-frequency Raman modes and electronic excitations in atomically thin MoS_2 films. *Phys. Rev. B* **2012**, *86*, 241301(R).

[116] Plechinger, G.; Heydrich, S.; Eroms, J.; Weiss, D.; Schüller, C.; Korn, T. Raman spectroscopy of the interlayer shear mode in few-layer MoS_2 flakes. *Appl. Phys. Lett.* **2012**, *101*, 101906.

[117] Lui, C. H.; Heinz, T. F. Measurement of layer breathing mode vibrations in few-layer graphene. *Phys. Rev. B* **2013**, *87*, 121404(R).

[118] Lui, C. H.; Ye, Z. P.; Keiser, C.; Xiao, X.; He, R. Temperature-activated layer-breathing vibrations in few-layer graphene. *Nano Lett.* **2014**, *14*, 4615–4621.

[119] Richter, H.; Wang, Z. P.; Ley, L. The one phonon Raman spectrum in microcrystalline silicon. *Solid State Commun.* **1981**, *39*, 625–629.

[120] Sun, Q.-C.; Mazumdar, D.; Yadgarov, L.; Rosentsveig, R.; Tenne, R.; Musfeldt, J. L. Spectroscopic determination of phonon lifetimes in rhenium-doped MoS_2 nanoparticles. *Nano Lett.* **2013**, *13*, 2803–2808.

[121] Yan, Y.; Zhou, X.; Jin, H.; Li, C.-Z.; Ke, X. X.; Van Tendeloo, G.; Liu, K. H.; Yu, D. P.; Dressel, M.; Liao, Z.-M. Surface-facet-dependent phonon deformation potential in individual strained topological insulator Bi_2Se_3 nanoribbons.

ACS Nano **2015**, *9*, 10244–10251.

[122] Wang, C. X.; Zhu, X. G.; Nilsson, L.; Wen, J.; Wang, G.; Shan, X. Y.; Zhang, Q.; Zhang, S. L.; Jia, J. F.; Xue, Q. K. *In situ* Raman spectroscopy of topological insulator Bi_2Te_3 films with varying thickness. *Nano Res.* **2013**, *6*, 688–692.

[123] Zhang, J.; Peng, Z. P.; Soni, A.; Zhao, Y. Y.; Xiong, Y.; Peng, B.; Wang, J. B.; Dresselhaus, M. S.; Xiong, Q. H. Raman spectroscopy of few-quintuple layer topological insulator Bi_2Se_3 nanoplatelets. *Nano Lett.* **2011**, *11*, 2407–2414.

[124] Mignuzzi, S.; Pollard, A. J.; Bonini, N.; Brennan, B.; Gilmore, I. S.; Pimenta, M. A.; Richards, D.; Roy, D. Effect of disorder on Raman scattering of single-layer MoS_2. *Phys. Rev. B* **2015**, *91*, 195411.

[125] Shi, W.; Lin, M.-L.; Tan, Q.-H.; Qiao, X.-F.; Zhang, J.; Tan, P.-H. Raman and photoluminescence spectra of two-dimensional nanocrystallites of monolayer WS_2 and WSe_2. *2D Mater.* **2016**, *3*, 025016.

[126] Wu, J.-B.; Zhao, H.; Li, Y. R.; Ohlberg, D.; Shi, W.; Wu, W.; Wang, H.; Tan, P.-H. Monolayer molybdenum disulfide nanoribbons with high optical anisotropy. *Adv. Opt. Mater.* **2016**, *4*, 756–762.

[127] Molina-Sánchez, A.; Wirtz, L. Phonons in single-layer and few-layer MoS_2 and WS_2. *Phys. Rev. B* **2011**, *84*, 155413.

[128] Campbell, I. H.; Fauchet, P. M. The effects of microcrystal size and shape on the one phonon Raman spectra of crystalline semiconductors. *Solid State Commun.* **1986**, *58*, 739–741.

[129] Khoo, K. H.; Zayak, A. T.; Kwak, H.; Chelikowsky, J. R. First-principles study of confinement effects on the raman spectra of Si nanocrystals. *Phys. Rev. Lett.* **2010**, *105*, 115504.

[130] Lu, W. L.; Nan, H. Y.; Hong, J. H.; Chen, Y. M.; Zhu, C.; Liang, Z.; Ma, X. Y.; Ni, Z. H.; Jin, C. H.; Zhang, Z. Plasma-assisted fabrication of monolayer phosphorene and its Raman characterization. *Nano Res.* **2014**, *7*, 853–859.

[131] Castellanos-Gomez, A.; Vicarelli, L.; Prada, E.; Island, J. O.; Narasimha-Acharya, K. L.; Blanter, S. I.; Groenendijk, D. J.; Buscema, M.; Steele, G. A.; Alvarez, J. V. et al. Isolation and characterization of few-layer black phosphorus. *2D Mater.* **2014**, *1*, 025001.

[132] Tonndorf, P.; Schmidt, R.; Böttger, P.; Zhang, X.; Börner, J.; Liebig, A.; Albrecht, M.; Kloc, C.; Gordan, O.; Zahn, D. R. T. et al. Photoluminescence emission and Raman response of monolayer MoS_2, $MoSe_2$, and WSe_2. *Opt. Express* **2013**, *21*, 4908–4916.

[133] Lee, C.; Yan, H. G.; Brus, L. E.; Heinz, T. F.; Hone, J.; Ryu, S. Anomalous lattice vibrations of single- and few-layer MoS_2. *ACS Nano* **2010**, *4*, 2695–2700.

[134] Zhao, W. J.; Ghorannevis, Z.; Amara, K. K.; Pang, J. R.; Toh, M.; Zhang, X.; Kloc, C.; Tan, P. H.; Eda, G. Lattice dynamics in mono- and few-layer sheets of WS_2 and WSe_2. *Nanoscale* **2013**, *5*, 9677–9683.

[135] Ling, X.; Liang, L. B.; Huang, S. X.; Puretzky, A. A.; Geohegan, D. B.; Sumpter, B. G.; Kong, J.; Meunier, V.; Dresselhaus, M. S. Low-frequency interlayer breathing modes in few-layer black phosphorus. *Nano Lett.* **2015**, *15*, 4080–4088.

[136] Dong, S.; Zhang, A. M.; Liu, K.; Ji, J. T.; Ye, Y. G.; Luo, X. G.; Chen, X. H.; Ma, X. L.; Jie, Y. H.; Chen, C. F. et al. Ultralow-frequency collective compression mode and strong interlayer coupling in multilayer black phosphorus. *Phys. Rev. Lett.* **2016**, *116*, 087401.

[137] Zhao, Y. Y.; Luo, X.; Zhang, J.; Wu, J. X.; Bai, X. X.; Wang, M. X.; Jia, J. F.; Peng, H. L.; Liu, Z. F.; Quek, S. Y. et al. Interlayer vibrational modes in few-quintuple-layer Bi_2Te_3 and Bi_2Se_3 two-dimensional crystals: Raman spectroscopy and first-principles studies. *Phys. Rev. B* **2014**, *90*, 245428.

[138] Chakraborty, B.; Bera, A.; Muthu, D. V. S.; Bhowmick, S.; Waghmare, U. V.; Sood, A. K. Symmetry-dependent phonon renormalization in monolayer MoS_2 transistor. *Phys. Rev. B* **2012**, *85*, 161403(R).

[139] Lazzeri, M.; Piscanec, S.; Mauri, F.; Ferrari, A. C.; Robertson, J. Phonon linewidths and electron–phonon coupling in graphite and nanotubes. *Phys. Rev. B* **2006**, *73*, 155426.

[140] Bonini, N.; Lazzeri, M.; Marzari, N.; Mauri, F. Phonon anharmonicities in graphite and graphene. *Phys. Rev. Lett.* **2007**, *99*, 176802.

[141] LaForge, A. D.; Frenzel, A.; Pursley, B. C.; Lin, T.; Liu, X. F.; Shi, J.; Basov, D. N. Optical characterization of Bi_2Se_3 in a magnetic field: Infrared evidence for magnetoelectric coupling in a topological insulator material. *Phys. Rev. B* **2010**, *81*, 125120.

[142] Di Pietro, P.; Ortolani, M.; Limaj, O.; Di Gaspare, A.; Giliberti, V.; Giorgianni, F.; Brahlek, M.; Bansal, N.; Koirala, N.; Oh, S. et al. Observation of Dirac plasmons in a topological insulator. *Nat. Nanotechnol.* **2013**, *8*, 556–560.

[143] Chen, C. Y.; Xie, Z. J.; Feng, Y.; Yi, H. M.; Liang, A. J.; He, S. L.; Mou, D. X.; He, J. F.; Peng, Y. Y.; Liu, X. et al. Tunable dirac fermion dynamics in topological insulators. *Sci. Rep.* **2013**, *3*, 2411.

[144] Costache, M. V.; Neumann, I.; Sierra, J. F.; Marinova, V.; Gospodinov, M. M.; Roche, S.; Valenzuela, S. O. Fingerprints of inelastic transport at the surface of the topological insulator Bi_2Se_3: Role of electron–phonon coupling. *Phys. Rev. Lett.* **2014**, *112*, 086601.

[145] Boukhicha, M.; Calandra, M.; Measson, M.-A.; Lancry, O.;

Shukla, A. Anharmonic phonons in few-layer MoS_2: Raman spectroscopy of ultralow energy compression and shear modes. *Phys. Rev. B* **2013**, *87*, 195316.

[146] Ji, J. T.; Zhang, A. M.; Fan, J. H.; Li, Y. S.; Wang, X. Q.; Zhang, J. D.; Plummer, E. W.; Zhang, Q. M. Giant magneto-optical Raman effect in a layered transition metal compound. *Proc. Natl. Acad. Sci. USA* **2016**, *113*, 2349–2353.

[147] Ling, X.; Huang, S. X.; Hasdeo, E. H.; Liang, L. B.; Parkin, W. M.; Tatsumi, Y.; Nugraha, A. R. T.; Puretzky, A. A.; Das, P. M.; Sumpter, B. G. et al. Anisotropic electron–photon and electron–phonon interactions in black phosphorus. *Nano Lett.* **2016**, *16*, 2260–2267.

[148] Li, H.; Zhang, Q.; Yap, C. C. R.; Tay, B. K.; Edwin, T. H. T.; Olivier, A.; Baillargeat, D. From bulk to monolayer MoS_2: Evolution of Raman scattering. *Adv. Funct. Mater.* **2012**, *22*, 1385–1390.

[149] Chen, S.-Y.; Zheng, C. X.; Fuhrer, M. S.; Yan, J. Helicity-resolved Raman scattering of MoS_2, $MoSe_2$, WS_2, and WSe_2 atomic layers. *Nano Lett.* **2015**, *15*, 2526–2532.

[150] Tongay, S.; Zhou, J.; Ataca, C.; Lo, K.; Matthews, T. S.; Li, J. B.; Grossman, J. C.; Wu, J. Q. Thermally driven crossover from indirect toward direct bandgap in 2D semiconductors: $MoSe_2$ versus MoS_2. *Nano Lett.* **2012**, *12*, 5576–5580.

[151] Lu, X.; Utama, M. I. B.; Lin, J. H.; Luo, X.; Zhao, Y. Y.; Zhang, J.; Pantelides, S. T.; Zhou, W.; Quek, S. Y.; Xiong, Q. H. Rapid and nondestructive identification of polytypism and stacking sequences in few-layer molybdenum diselenide by Raman spectroscopy. *Adv. Mater.* **2015**, *27*, 4502–4508.

[152] Ruppert, C.; Aslan, O. B.; Heinz, T. F. Optical properties and band gap of single- and few-layer $MoTe_2$ crystals. *Nano Lett.* **2014**, *14*, 6231–6236.

[153] Yamamoto, M.; Wang, S. T.; Ni, M. Y.; Lin, Y. F.; Li, S. L.; Aikawa, S.; Jian, W. B.; Ueno, K.; Wakabayashi, K.; Tsukagoshi, K. Strong enhancement of raman scattering from a bulk-inactive vibrational mode in few-layer $MoTe_2$. *ACS Nano* **2014**, *8*, 3895–3903.

[154] Li, H.; Lu, G.; Wang, Y. L.; Yin, Z. Y.; Cong, C. X.; He, Q. Y.; Wang, L.; Ding, F.; Yu, T.; Zhang, H. Mechanical exfoliation and characterization of single- and few-layer nanosheets of WSe_2, TaS_2, and $TaSe_2$. *Small* **2013**, *9*, 1974–1981.

[155] Terrones, H.; Del Corro, E.; Feng, S.; Poumirol, J. M.; Rhodes, D.; Smirnov, D.; Pradhan, N. R.; Lin, Z.; Nguyen, M. A. T.; Elias, A. L. et al. New first order raman-active modes in few layered transition metal dichalcogenides. *Sci. Rep.* **2014**, *4*, 4215.

[156] Huang, J.-K.; Pu, J.; Hsu, C.-L.; Chiu, M.-H.; Juang, Z.-Y.; Chang, Y.-H.; Chang, W.-H.; Iwasa, Y.; Takenobu, T.; Li, L.-J. Large-area synthesis of highly crystalline WSe_2 monolayers and device applications. *ACS Nano* **2014**, *8*, 923–930.

[157] Mrstik, B. J.; Kaplan, R.; Reinecke, T. L.; Van Hove, M.; Tong, S. Y. Surface-structure determination of the layered compounds MoS_2 and $NbSe_2$ by low-energy electron diffraction. *Phys. Rev. B* **1977**, *15*, 897–900.

[158] Liu, K. K.; Zhang, W. J.; Lee, Y. H.; Lin, Y. C.; Chang, M. T.; Su, C. Y.; Chang, C. S.; Li, H.; Shi, Y. M.; Zhang, H. et al. Growth of large-area and highly crystalline MoS_2 thin layers on insulating substrates. *Nano Lett.* **2012**, *12*, 1538–1544.

[159] Castellanos-Gomez, A.; Barkelid, M.; Goossens, A. M.; Calado, V. E.; van der Zant, H. S. J.; Steele, G. A. Laser-thinning of MoS_2: On demand generation of a single-layer semiconductor. *Nano Lett.* **2012**, *12*, 3187–3192.

[160] Lu, X.; Utama, M. I. B.; Zhang, J.; Zhao, Y. Y.; Xiong, Q. H. Layer-by-layer thinning of MoS_2 by thermal annealing. *Nanoscale* **2013**, *5*, 8904–8908.

[161] Lin, Y. X.; Ling, X.; Yu, L. L.; Huang, S. X.; Hsu, A. L.; Lee, Y. H.; Kong, J.; Dresselhaus, M. S.; Palacios, T. Dielectric screening of excitons and trions in single-layer MoS_2. *Nano Lett.* **2014**, *14*, 5569–5576.

[162] Froehlicher, G.; Lorchat, E.; Fernique, F.; Joshi, C.; Molina-Sánchez, A.; Wirtz, L.; Berciaud, S. Unified description of the optical phonon modes in N-layer $MoTe_2$. *Nano Lett.* **2015**, *15*, 6481–6489.

[163] Kim, Y.; Jhon, Y. I.; Park, J.; Kim, J. H.; Lee, S.; Jhon, Y. M. Anomalous Raman scattering and lattice dynamics in mono- and few-layer WTe_2. *Nanoscale* **2016**, *8*, 2309–2316.

[164] Shulenburger, L.; Baczewski, A. D.; Zhu, Z.; Guan, J.; Tománek, D. The nature of the interlayer interaction in bulk and few-layer phosphorus. *Nano Lett.* **2015**, *15*, 8170–8175.

[165] Luo, N. S.; Ruggerone, P.; Toennies, J. P. Theory of surface vibrations in epitaxial thin films. *Phys. Rev. B* **1996**, *54*, 5051–5063.

[166] Zhao, Y. Y.; de la Mata, M.; Qiu, R. L. J.; Zhang, J.; Wen, X. L.; Magen, C.; Gao, X. P. A.; Arbiol, J.; Xiong, Q. H. Te-seeded growth of few-quintuple layer Bi_2Te_3 nanoplates. *Nano Res.* **2014**, *7*, 1243–1253.

[167] Buscema, M.; Steele, G. A.; van der Zant, H. S. J.; Castellanos-Gomez, A. The effect of the substrate on the Raman and photoluminescence emission of single-layer MoS_2. *Nano Res.* **2014**, *7*, 561–571.

[168] Lui, C. H.; Ye, Z. P.; Ji, C.; Chiu, K.-C.; Chou, C.-T.; Andersen, T. I.; Means-Shively, C.; Anderson, H.; Wu, J.-M.; Kidd, T. et al. Observation of interlayer phonon modes in van der Waals heterostructures. *Phys. Rev. B* **2015**, *91*, 165403.

[169] Wang, H.; Feng, M.; Zhang, X.; Tan, P.-H.; Wang, Y. F. In-phase family and self-similarity of interlayer vibrational frequencies in van der Waals layered materials. *J. Phys. Chem. C* **2015**, *119*, 6906–6911.

[170] Wu, J.-B.; Hu, Z.-X.; Zhang, X.; Han, W.-P.; Lu, Y.; Shi, W.; Qiao, X.-F.; Ijiäs, M.; Milana, S.; Ji, W. et al. Interface coupling in twisted multilayer graphene by resonant raman spectroscopy of layer breathing modes. *ACS Nano* **2015**, *9*, 7440–7449.

[171] Li, Y. L.; Rao, Y.; Mak, K. F.; You, Y. M.; Wang, S. Y.; Dean, C. R.; Heinz, T. F. Probing symmetry properties of few-layer MoS_2 and h-BN by optical second-harmonic generation. *Nano Lett.* **2013**, *13*, 3329–3333.

[172] Kappera, R.; Voiry, D.; Yalcin, S. E.; Branch, B.; Gupta, G.; Mohite, A. D.; Chhowalla, M. Phase-engineered low-resistance contacts for ultrathin MoS_2 transistors. *Nat. Mater.* **2014**, *13*, 1128–1134.

[173] He, J. G.; Hummer, K.; Franchini, C. Stacking effects on the electronic and optical properties of bilayer transition metal dichalcogenides MoS_2, $MoSe_2$, WS_2, and WSe_2. *Phys. Rev. B* **2014**, *89*, 075409.

[174] Huang, S. X.; Ling, X.; Liang, L. B.; Kong, J.; Terrones, H.; Meunier, V.; Dresselhaus, M. S. Probing the interlayer coupling of twisted bilayer MoS_2 using photoluminescence spectroscopy. *Nano Lett.* **2014**, *14*, 5500–5508.

[175] Jiang, T.; Liu, H. R.; Huang, D.; Zhang, S.; Li, Y. G.; Gong, X.; Shen, Y.-R.; Liu, W.-T.; Wu, S. W. Valley and band structure engineering of folded MoS_2 bilayers. *Nat. Nanotechnol.* **2014**, *9*, 825–829.

[176] Zhang, L. M.; Liu, K. H.; Wong, A. B.; Kim, J.; Hong, X. P.; Liu, C.; Cao, T.; Louie, S. G.; Wang, F.; Yang, P. D. Three-dimensional spirals of atomic layered MoS_2. *Nano Lett.* **2014**, *14*, 6418–6423.

[177] Plechinger, G.; Mooshammer, F.; Castellanos-Gomez, A.; Steele, G. A.; Schüller, C.; Korn, T. Optical spectroscopy of interlayer coupling in artificially stacked MoS_2 layers. *2D Mater.* **2015**, *2*, 034016.

[178] Fang, H.; Battaglia, C.; Carraro, C.; Nemsak, S.; Ozdol, B.; Kang, J. S.; Bechtel, H. A.; Desai, S. B.; Kronast, F.; Unal, A. A. et al. Strong interlayer coupling in van der Waals heterostructures built from single-layer chalcogenides. *Proc. Natl. Acad. Sci. USA* **2014**, *111*, 6198–6202.

[179] Zhang, J.; Wang, J. H.; Chen, P.; Sun, Y.; Wu, S.; Jia, Z. Y.; Lu, X. B.; Yu, H.; Chen, W.; Zhu, J. Q. et al. Observation of strong interlayer coupling in MoS_2/WS_2 heterostructures. *Adv. Mater.* **2016**, *28*, 1950–1956.

[180] Puretzky, A. A.; Liang, L. B.; Li, X. F.; Xiao, K.; Wang, K.; Mahjouri-Samani, M.; Basile, L.; Idrobo, J. C.; Sumpter, B. G.; Meunier, V. et al. Low-frequency raman fingerprints of two-dimensional metal dichalcogenide layer stacking configurations. *ACS Nano* **2015**, *9*, 6333–6342.

[181] Yan, J. X.; Xia, J.; Wang, X. L.; Liu, L.; Kuo, J.-L.; Tay, B. K.; Chen, S. S.; Zhou, W.; Liu, Z.; Shen, Z. X. Stacking-dependent interlayer coupling in trilayer MoS_2 with broken inversion symmetry. *Nano Lett.* **2015**, *15*, 8155–8161.

[182] Puretzky, A. A.; Liang, L. B.; Li, X. F.; Xiao, K.; Sumpter, B. G.; Meunier, V.; Geohegan, D. B. Twisted $MoSe_2$ bilayers with variable local stacking and interlayer coupling revealed by low-frequency raman spectroscopy. *ACS Nano* **2016**, *10*, 2736–2744.

[183] Huang, S. X.; Liang, L. B.; Ling, X.; Puretzky, A. A.; Geohegan, D. B.; Sumpter, B. G.; Kong, J.; Meunier, V.; Dresselhaul, M. S. Low-frequency interlayer Raman modes to probe interface of twisted bilayer MoS_2. *Nano Lett.* **2016**, *16*, 1435–1444.

[184] Luo, X.; Lu, X.; Cong, C. X.; Yu, T.; Xiong, Q. H.; Quek, S. Y. Stacking sequence determines Raman intensities of observed interlayer shear modes in 2D layered materials—A general bond polarizability model. *Sci. Rep.* **2015**, *5*, 14565.

[185] Guha, S.; Menéndez, J.; Page, J. B.; Adams, G. B. Empirical bond polarizability model for fullerenes. *Phys. Rev. B* **1996**, *53*, 13106–13114.

[186] Utama, M. I. B.; Lu, X.; Yuan, Y. W.; Xiong, Q. H. Detrimental influence of catalyst seeding on the device properties of CVD-grown 2D layered materials: A case study on $MoSe_2$. *Appl. Phys. Lett.* **2014**, *105*, 253102.

[187] Lui, C. H.; Ye, Z. P.; Keiser, C.; Barros, E. B.; He, R. Stacking-dependent shear modes in trilayer graphene. *Appl. Phys. Lett.* **2015**, *106*, 041904

[188] Zhang, X.; Han, W.-P.; Qiao, X.-F.; Tan, Q.-H.; Wang, Y.-F.; Zhang, J.; Tan, P.-H. Raman characterization of AB- and ABC-stacked few-layer graphene by interlayer shear modes. *Carbon* **2016**, *99*, 118–122.

[189] Lee, J.-U.; Kim, K.; Han, S.; Ryu, G. H.; Lee, Z.; Cheong, H. Raman signatures of polytypism in molybdenum disulfide. *ACS Nano* **2016**, *10*, 1948–1953.

[190] He, R.; Yan, J.-A.; Yin, Z. Y.; Ye, Z. P.; Ye, G. H.; Cheng, J.; Li, J.; Lui, C. H. Coupling and stacking order of ReS_2 atomic layers revealed by ultralow-frequency Raman spectroscopy. *Nano Lett.* **2016**, *16*, 1404–1409.

[191] Qiao, X.-F.; Wu, J.-B.; Zhou, L. W.; Qiao, J. S.; Shi, W.; Chen, T.; Zhang, X.; Zhang, J.; Ji, W.; Tan, P.-H. Polytypism and unexpected strong interlayer coupling in two-dimensional layered ReS_2. *Nanoscale* **2016**, *8*, 8324–8332.

[192] Chenet, D. A.; Aslan, O. B.; Huang, P. Y.; Fan, C.; van der Zande, A. M.; Heinz, T. F.; Hone, J. C. In-plane anisotropy in mono- and few-layer ReS_2 probed by raman spectroscopy and scanning transmission electron microscopy. *Nano Lett.*

2015, *15*, 5667–5672.

[193] Wolverson, D.; Crampin, S.; Kazemi, A. S.; Ilie, A.; Bending, S. J. Raman spectra of monolayer, few-layer, and bulk $ReSe_2$: An anisotropic layered semiconductor. *ACS Nano* **2014**, *8*, 11154–11164.

[194] Zhao, H.; Wu, J. B.; Zhong, H. X.; Guo, Q. S.; Wang, X. M.; Xia, F. N.; Yang, L.; Tan, P. H.; Wang, H. Interlayer interactions in anisotropic atomically thin rhenium diselenide. *Nano Res.* **2015**, *8*, 3651–3661.

[195] Ribeiro, H. B.; Pimenta, M. A.; de Matos, C. J. S.; Moreira, R. L.; Rodin, A. S.; Zapata, J. D.; de Souza, E. A. T.; Castro Neto, A. H. Unusual angular dependence of the raman response in black phosphorus. *ACS Nano* **2015**, *9*, 4270–4276.

[196] Cai, Y. Q.; Ke, Q. Q.; Zhang, G.; Feng, Y. P.; Shenoy, V. B.; Zhang, Y.-W. Giant phononic anisotropy and unusual anharmonicity of phosphorene: Interlayer coupling and strain engineering. *Adv. Funct. Mater.* **2015**, *25*, 2230–2236.

[197] Wu, J. X.; Mao, N. N.; Xie, L. M.; Xu, H.; Zhang, J. Identifying the crystalline orientation of black phosphorus using angle-resolved polarized Raman spectroscopy. *Angew. Chem., Int. Ed.* **2015**, *54*, 2366–2369.

[198] Zhu, B. R.; Zeng, H. L.; Dai, J. F.; Gong, Z. R.; Cui, X. D. Anomalously robust valley polarization and valley coherence in bilayer WS_2. *Proc. Natl. Acad. Sci. USA* **2014**, *111*, 11606–11611.

[199] Jones, A. M.; Yu, H. Y.; Ghimire, N. J.; Wu, S. F.; Aivazian, G.; Ross, J. S.; Zhao, B.; Yan, J. Q.; Mandrus, D. G.; Xiao, D. et al. Optical generation of excitonic valley coherence in monolayer WSe_2. *Nat. Nanotechnol.* **2013**, *8*, 634–638.

[200] Efremov, E. V.; Ariese, F.; Gooijer, C. Achievements in resonance Raman spectroscopy: Review of a technique with a distinct analytical chemistry potential. *Anal. Chim. Acta* **2008**, *606*, 119–134.

[201] Fan, J.-H.; Gao, P.; Zhang, A.-M.; Zhu, B.-R.; Zeng, H.-L.; Cui, X.-D.; He, R.; Zhang, Q.-M. Resonance Raman scattering in bulk 2H-MX_2 (M = Mo, W; X = S, Se) and monolayer MoS_2. *J. Appl. Phys.* **2014**, *115*, 053527.

[202] Cong, C. X.; Shang, J. Z.; Wu, X.; Cao, B. C.; Peimyoo, N.; Qiu, C. Y.; Sun, L. T.; Yu, T. Synthesis and optical properties of large-area single-crystalline 2D semiconductor WS_2 monolayer from chemical vapor deposition. *Adv. Opt. Mater.* **2014**, *2*, 131–136.

[203] Chakraborty, B.; Matte, H. S. S. R.; Sood, A. K.; Rao, C. N. R. Layer-dependent resonant Raman scattering of a few layer MoS_2. *J. Raman Spectrosc.* **2013**, *44*, 92–96.

[204] Lee, J.-U.; Park, J.; Son, Y.-W.; Cheong, H. Anomalous excitonic resonance Raman effects in few-layered MoS_2. *Nanoscale* **2015**, *7*, 3229–3236.

[205] Staiger, M.; Gillen, R.; Scheuschner, N.; Ochedowski, O.; Kampmann, F.; Schleberger, M.; Thomsen, C.; Maultzsch, J. Splitting of monolayer out-of-plane A_1' Raman mode in few-layer WS_2. *Phys. Rev. B* **2015**, *91*, 195419.

[206] Schuller, J. A.; Karaveli, S.; Schiros, T.; He, K. L.; Yang, S. Y.; Kymissis, I.; Shan, J.; Zia, R. Orientation of luminescent excitons in layered nanomaterials. *Nat. Nanotechnol.* **2013**, *8*, 271–276.

[207] Molina-Sánchez, A.; Sangalli, D.; Hummer, K.; Marini, A.; Wirtz, L. Effect of spin-orbit interaction on the optical spectra of single-layer, double-layer, and bulk MoS_2. *Phys. Rev. B* **2013**, *88*, 045412.

[208] Carvalho, B. R.; Malard, L. M.; Alves, J. M.; Fantini, C.; Pimenta, M. A. Symmetry-dependent exciton-phonon coupling in 2D and bulk MoS_2 observed by resonance Raman scattering. *Phys. Rev. Lett.* **2015**, *114*, 136403.

[209] Nam, D.; Lee, J.-U.; Cheong, H. Excitation energy dependent Raman spectrum of $MoSe_2$. *Sci. Rep.* **2015**, *5*, 17113.

[210] Scheuschner, N.; Gillen, R.; Staiger, M.; Maultzsch, J. Interlayer resonant Raman modes in few-layer MoS_2. *Phys. Rev. B* **2015**, *91*, 235409.

[211] del Corro, E.; Terrones, H.; Elias, A.; Fantini, C.; Feng, S. M.; Nguyen, M. A.; Mallouk, T. E.; Terrones, M.; Pimenta, M. A. Excited excitonic states in 1 L, 2 L, 3 L, and bulk WSe_2 observed by resonant Raman spectroscopy. *ACS Nano* **2014**, *8*, 9629–9635.

[212] del Corro, E.; Botello-Méndez, A.; Gillet, Y.; Elias, A. L.; Terrones, H.; Feng, S.; Fantini, C.; Rhodes, D.; Pradhan, N.; Balicas, L. et al. Atypical exciton−phonon interactions in WS_2 and WSe_2 monolayers revealed by resonance Raman spectroscopy. *Nano Lett.* **2016**, *16*, 2363–2368.

[213] Song, Q. J.; Tan, Q. H.; Zhang, X.; Wu, J. B.; Sheng, B. W.; Wan, Y.; Wang, X. Q.; Dai, L.; Tan, P. H. Physical origin of Davydov splitting and resonant Raman spectroscopy of Davydov components in multilayer $MoTe_2$. *Phys. Rev. B* **2016**, *93*, 115409.

[214] Ferrari, A. C.; Meyer, J. C.; Scardaci, V.; Casiraghi, C.; Lazzeri, M.; Mauri, F.; Piscanec, S.; Jiang, D.; Novoselov, K. S.; Roth, S. et al. Raman spectrum of graphene and graphene layers. *Phys. Rev. Lett.* **2006**, *97*, 187401.

[215] Dresselhaus, M. S.; Jorio, A.; Hofmann, M.; Dresselhaus, G.; Saito, R. Perspectives on carbon nanotubes and graphene Raman spectroscopy. *Nano Lett.* **2010**, *10*, 751–758.

[216] Venezuela, P.; Lazzeri, M.; Mauri, F. Theory of double-resonant Raman spectra in graphene: Intensity and line shape of defect-induced and two-phonon bands. *Phys. Rev. B* **2011**, *84*, 035433.

[217] Wang, G.; Glazov, M. M.; Robert, C.; Amand, T.; Marie, X.; Urbaszek, B. Double resonant Raman scattering and valley coherence generation in monolayer WSe_2. *Phys. Rev. Lett.*

2015, *115*, 117401.

[218] Sun, L. F.; Yan, J. X.; Zhan, D.; Liu, L.; Hu, H. L.; Li, H.; Tay, B. K.; Kuo, J.-L.; Huang, C.-C.; Hewak, D. W. et al. Spin-orbit splitting in single-layer MoS_2 revealed by triply resonant Raman scattering. *Phys. Rev. Lett.* **2013**, *111*, 126801.

[219] Lanzillo, N. A.; Birdwell, A. G.; Amani, M.; Crowne, F. J.; Shah, P. B.; Najmaei, S.; Liu, Z.; Ajayan, P. M.; Lou, J.; Dubey, M. et al. Temperature-dependent phonon shifts in monolayer MoS_2. *Appl. Phys. Lett.* **2013**, *103*, 093102.

[220] Thripuranthaka, M.; Late, D. J. Temperature dependent phonon shifts in single-layer WS_2. *ACS Appl. Mater. Interfaces* **2014**, *6*, 1158–1163.

[221] Late, D. J. Temperature dependent phonon shifts in few-layer black phosphorus. *ACS Appl. Mater. Interfaces* **2015**, *7*, 5857–5862.

[222] Peimyoo, N.; Shang, J. Z.; Yang, W. H.; Wang, Y. L.; Cong, C. X.; Yu, T. Thermal conductivity determination of suspended mono- and bilayer WS_2 by Raman spectroscopy. *Nano Res.* **2015**, *8*, 1210–1221.

[223] Chi, Z.-H.; Zhao, X.-M.; Zhang, H. D.; Goncharov, A. F.; Lobanov, S. S.; Kagayama, T.; Sakata, M.; Chen, X.-J. Pressure-induced metallization of molybdenum disulfide. *Phys. Rev. Lett.* **2014**, *113*, 036802.

[224] Fan, W.; Zhu, X.; Ke, F.; Chen, Y. B.; Dong, K. C.; Ji, J.; Chen, B.; Tongay, S.; Ager, J. W.; Liu, K. et al. Vibrational spectrum renormalization by enforced coupling across the van der Waals gap between MoS_2 and WS_2 monolayers. *Phys. Rev. B* **2015**, *92*, 241408(R).

[225] Chang, C.-H.; Fan, X. F.; Lin, S.-H.; Kuo, J.-L. Orbital analysis of electronic structure and phonon dispersion in MoS_2, $MoSe_2$, WS_2, and WSe_2 monolayers under strain. *Phys. Rev. B* **2013**, *88*, 195420.

[226] Zhu, C. R.; Wang, G.; Liu, B. L.; Marie, X.; Qiao, X. F.; Zhang, X.; Wu, X. X.; Fan, H.; Tan, P. H.; Amand, T. et al. Strain tuning of optical emission energy and polarization in monolayer and bilayer MoS_2. *Phys. Rev. B* **2013**, *88*, 121301(R).

[227] Wang, Y. L.; Cong, C. X.; Qiu, C. Y.; Yu, T. Raman spectroscopy study of lattice vibration and crystallographic orientation of monolayer MoS_2 under uniaxial strain. *Small* **2013**, *9*, 2857–2861.

[228] Wang, Y. L.; Cong, C. X.; Yang, W. H.; Shang, J. Z.; Peimyoo, N.; Chen, Y.; Kang, J. Y.; Wang, J. P.; Huang, W.; Yu, T. Strain-induced direct–indirect bandgap transition and phonon modulation in monolayer WS_2. *Nano Res.* **2015**, *8*, 2562–2572.

[229] Das, A.; Pisana, S.; Chakraborty, B.; Piscanec, S.; Saha, S. K.; Waghmare, U. V.; Novoselov, K. S.; Krishnamurthy, H. R.; Geim, A. K.; Ferrari, A. C. et al. Monitoring dopants by Raman scattering in an electrochemically top-gated graphene transistor. *Nat. Nanotechnol.* **2008**, *3*, 210–215.

[230] Das, A.; Sood, A. K.; Govindaraj, A.; Saitta, A. M.; Lazzeri, M.; Mauri, F.; Rao, C. N. R. Doping in carbon nanotubes probed by Raman and transport measurements. *Phys. Rev. Lett.* **2007**, *99*, 136803.

[231] Chakraborty, B.; Gupta, S. N.; Singh, A.; Kuiri, M.; Kumar, C.; Muthu, D. V. S.; Das, A.; Waghmare, U. V.; Sood, A. K. Electron–hole asymmetry in the electron–phonon coupling in top-gated phosphorene transistor. *2D Mater.* **2016**, *3*, 015008.

[232] Withers, F.; Del Pozo-Zamudio, O.; Mishchenko, A.; Rooney, A. P.; Gholinia, A.; Watanabe, K.; Taniguchi, T.; Haigh, S. J.; Geim, A. K.; Tartakovskii, A. I. et al. Light-emitting diodes by band-structure engineering in van der Waals heterostructures. *Nat. Mater.* **2015**, *14*, 301–306.